UNIVERSITÄT ROSTOCK

Analytical modelling of the ecosystem within an oxygen minimum zone under the influence of wind driven upwelling

Masterthesis in physics

written at the

Leibniz Institut für Ostseeforschung Warnemünde

handed in at the

Institut für Physik der Universität Rostock

Academic advisor:
Dr. Martin Schmidt
Second examiner :
Dr. René Friedland

Student:
Martin Mohrmann

March 11, 2015

Abstract

An analytical model for wind driven upwelling and the resulting ecosystem response is derived in this thesis. Beginning with the linearised Boussinesq equations, the response of the ocean to windforcing is analysed. Especially wind fields with a rotational wind stress are of interest due to their strong upwelling. The resulting hydrodynamic equations, describing the upwelling, are used as an input to an analytical ecosystem model within a circular, rotational wind field.
The model ecosystem is located in the open ocean exchanging tracers with the surrounding water by advection. Detritus, nutrients and oxygen are considered in the model including advection, mineralisation of detritus and (in some cases) diffusion. These model components are sufficient to describe the formation of an oxygen minimum zone and the nutrient enrichment within an upwelling area.
The analytic procedure of solution allows a consistent description of the processes within an upwelling area. The connection of physical properties like the wind stress and the depth of the water are directly linked to tracer equations of the ecosystem model. The effect of different assumptions about the boundary conditions and fluxes are discussed.

Zusammenfassung

Ein analytisches Modell von windgetriebenem Upwelling und der Reaktion des Ökosystemes wird in dieser Arbeit hergeleitet. Beginnend mit den linearisierten Boussinesqgleichungen wird die Reaktion des Ozeans auf Windantriebe beschrieben. Besondere Aufmerksamkeit erfahren dabei Windantriebe mit Rotationsanteil, da diese starkes Upwelling verursachen. Die resultierenden hydrodynamischen Gleichungen, welche die Strömungen unter Windantrieb beschreiben, sind die Basis der Advektionsterme in einem einfachen Ökosystemmodell.
Das Ökosystem befinde sich im Ozean und tauscht über die berechneten Strömungen Tracerkonzentrationen mit seiner Umgebung aus. Das einfache Modell verfolgt die Tracer Sauerstoff, Nährstoffe und Detritus und beinhaltet Advektion, Detritusmineralisierung und (teilweise) Diffusionsterme. Diese Modellkomponenten sind hinreichend, um die Entstehung einer Sauerstoffminimumzone und der Nährstoffanreicherung in einem Upwellinggebiet zu beschreiben.
Die analytische Herangehensweise erlaubt eine konsistente Beschreibung der stattfindenden Prozesse. Der Zusammenhang von physikalischen Parametern wie der Windstärke oder der Absinkgeschwindigkeit des Detritus wird in direkten Zusammenhang mit den Tracerkonzentrationen gebracht. Der Effekt verschiedener Randbedingungen auf das System wird untersucht und diskutiert.

Contents

1 Introduction

The global ocean circulation is transporting water masses over the distance of thousands of kilometers. When this water is advected into the euphotic zone of the ocean, it can play out its effect on the ecosystem. The deep water is often rich in nutrients and oxygen, a mixing into the surface layer can lead to a high ecosystem activity (e.g. O'Brien 1975). According to the formula for Ekman pumping

$$w(-H_{mix}) = -\mathrm{curl_z}\left(\frac{\tau}{f\rho_0}\right), \tag{1}$$

wind with a rotational structure has the potential to cause large scale upwelling (e.g. Olbers, Willebrand, and Eden 2012,p. 449). It is deemed to be responsible for some of the upwelling near the eastern coasts of the Atlantic ocean (e.g. M. Schmidt et al. 2000). Because of the low vertical velocities, the in-depth structure of the vertical velocity profiles is hard to measure (e.g. Kadko and Johns 2011). An analytical model for wind driven upwelling areas based on the linearised Boussinesq equations is developed in this thesis and employed for different wind structures.

The upwelling velocities are usually low in comparison to the horizontal velocities, but due to the strong vertical tracer gradients this process is of great importance for the ecosystem.

With simple analytical model components, the development of an oxygen minimum zone and the nutrient enrichment within an upwelling area are explained and analyzed.

The analytical theory does not allow a description of all effects in detail and the discussed equations may seem very simplified sometimes. It can not be the purpose of an analytical model to compete with numerical models in terms of the number of considered processes or the accuracy of reproduction of measurement profiles. The equations have to be simplified enough, to allow an analytical treatment.

The beauty of the analytical method however, is the direct visibility of the influence of different parameters on the result. In the end, a consistent description of the effect of upwelling in the hydrodynamic model on the ecosystem model is given. The influence of changed parameters in the wind field or different boundary conditions are directly derived from the descriptive equations, without the detour of employing a numerical model.

Based on the results of the hydrodynamical model equations, the advective exchange of the upwelling area with the surrounding ocean is considered. An analytical ecosystem model for polar symmetric wind forcings is derived.

2 A Physical Model of Wind Driven Upwelling

Compared to the lateral velocities, the vertical (up- and downwelling) velocities are usually two or three orders of magnitude smaller (Vélez-Belchí and Tintorí 2001). Still they are of great importance for the transport of state variables of the water. Vertical concentration gradients are much stronger than horizontal gradients in the water, already small upwelling velocities can change the attributes of the water in an important way.
In the range of wind-driven upwelling in the open ocean, there are two important processes that can cause upwelling. The first one is a time-dependent divergent wind stress at the surface, the second one is a rotational wind stress (1). For the ecosystem model, we are mainly interested in long term (or even steady state) upwelling effects caused by rotational wind forcings.

2.1 Table of Variables and Abbreviations for the Hydrodynamic Model

In order to keep the terms in the following derivations short and readable, a set of abbreviations is used. A table of variables and abbreviations is given here.

symbol	**meaning**
z	depth coordinate (z=0 at the surface, upwards positive)
ρ	radial polar coordinate
φ	angular polar coordinate
u, v	zonal/meridional velocity
w	vertical velocity (upwards positive)
H	depth of the ocean (H is positive)
H_{mix}	depth of the mixed layer (positive)
p	pressure
ϱ	density
f	Coriolis parameter
η	surface elevation
g	gravity of earth constant
b	buoyancy
$(X, Y), (R, \Phi)$	wind induced volume force in Cartesian/polar coordinates
N	Brunt-Väisälä frequency
n	mode index
$\vec{\tau}$	wind stress vector

2.2 Basic Equations and Approximations

As mentioned in the introduction, analytical modelling requires usually more simplified systems than numerical modelling. An analytical solution to the complete Navier-Stokes equations has yet to be found. Luckily, many effects are too small to cause a noticeable effect or can be omitted under certain conditions. Some of the approximations limit the applicability of the model in terms of the bottom topography, the lateral extend of the wind stress considered or the temporal variability of the processes.

The basic equations for the derivations in this chapter are the linearised Boussinesq-equations as written in (5). In this work, the Coriolis force is approximated by the f-plane approximation. Further approximations are the incompressibility of the water, and the Boussinesq approximation itself. At the time $t = 0$, an ocean at rest is assumed, without any currents or pressure perturbations existent.

2.3 The Boussinesq Equations

A starting point for the derivations are the linearized Boussinesq equations, as found in Fennel and Lass 1989.

$$\begin{aligned} \frac{\partial u}{\partial t} - fv + \frac{\partial p}{\partial x} &= X \\ \frac{\partial v}{\partial t} + fu + \frac{\partial p}{\partial y} &= Y \\ \frac{\partial p}{\partial z} - b &= 0 \end{aligned} \tag{2}$$

Additionally we use the continuity equation

$$\frac{\partial u}{\partial x} + \frac{\partial v}{\partial y} + \frac{\partial w}{\partial z} = 0 \tag{3}$$

and

$$\frac{\partial b}{\partial t} + N^2 w = 0. \tag{4}$$

If there is no risk of confusing the indices with derivatives, the derivatives are written in

a short notation by:

$$\begin{aligned} u_t - fv + p_x &= X \\ v_t + fu + p_y &= Y \\ -b + p_z &= 0 \\ b_t + N^2 w &= 0 \\ u_x + v_y + w_z &= 0 \end{aligned} \tag{5}$$

2.4 Initial Conditions

In the hydrodynamic model equations, a couple of initial conditions are used. At the time t=0, the ocean is at rest and there are no pressure perturbations, thus

$$u(t_0) = 0, \quad v(t_0) = 0, \quad p(t_0) = 0. \tag{6}$$

For later use, we require that the effects far away from the wind field vanish.

$$\begin{aligned} p(x_\infty) = \quad 0, p(y_\infty) = \quad 0 \\ u(x_\infty) = \quad 0, v(y_\infty) = \quad 0 \\ u_x(x_\infty) = \quad 0, v_y(y_\infty) = \quad 0 \end{aligned} \tag{7}$$

With this assumptions, it is easy to derive the following conditions in the ocean only with the help of the momentum equation and the continuity equation.

$$\begin{aligned} p_t(t_0) = 0, \qquad u_t(t_0) = X(t_0), \qquad v_t(t_0) = Y(t_0) \\ u_y(t_0) = 0, \qquad v_x(t_0) = 0 \\ p_{tt}(t_0) = -\lambda^{-2}(u_{xt}(t_0) + v_{yt}(t_0)) = -\lambda^{-2}\left[X_x(t_0) + Y_y(t_0)\right] \\ p_x(x_\infty) = 0, \qquad p_y(y_\infty) = 0 \end{aligned} \tag{8}$$

2.5 Decoupling the Boussinesq Equations in Cylindrical Geometry using Fourier Transformation

The starting point are the Boussinesq equations in cylindrical coordinates. Using Fourier transformations, we can get a single decoupled differential equation of the pressure p. Once the solution for the pressure equations is found, the velocities w, u^ρ, u^φ can be derived with the help of the Boussinesq equations. Starting with equation set (5), the

buoyancy can be eliminated and for a constant Brunt-Väisälä frequency, the equations in cylindrical coordinates are

$$\begin{aligned} u_t^\rho - f u^\varphi + p_\rho &= R \\ u_t^\varphi + f u^\rho + \frac{1}{\rho} p_\varphi &= \Phi \\ \frac{1}{\rho}\frac{\partial}{\partial \rho}\rho u^\rho + \frac{1}{\rho} u_\varphi^\varphi + w_z &= 0 \\ p_{tz} &= -N^2 w. \end{aligned} \tag{9}$$

In equation set (9), the new variables u^ρ and R are the radial velocity and the radial (outwards/inwards directed) part of the wind forcing. The variables u^φ and Φ are the angular velocity and the angular part of the windforcing. For the wind fields the conversion formulas

$$\begin{aligned} R &= Y \sin(\varphi) + X \cos(\varphi) \\ \Phi &= Y \cos(\varphi) - X \sin(\varphi) \end{aligned} \tag{10}$$

can be used to transform between Cartesian and cylindrical coordinates.

Multiplication of the first two equations of (9) with f and subtraction of the time derivative of the other equation respectively decouples the equations of u^ρ and u^φ. After Fourier transformation, the equations can be solved for one of the variables. Throughout this whole work, the definition for the Fourier transformations

$$\begin{aligned} \int_{-\infty}^{\infty} \mathrm{d}t\, \mathrm{d}\varphi\, e^{i\omega t - ik\varphi} F(\varphi, t) &= F(\omega, k) \\ \int_{-\infty}^{\infty} \frac{\mathrm{d}\omega}{2\pi} \frac{\mathrm{d}k}{2\pi} e^{-i\omega t + ik\varphi} F(k, \omega) &= F(\varphi, t) \end{aligned} \tag{11}$$

is used. For the velocity components, we get

$$\begin{aligned} u^\varphi &= \frac{1}{f^2 - \omega^2}\left(\left[\frac{i\omega}{\rho} im + f\frac{\partial}{\partial \rho}\right] p - i\omega\Phi - fR\right) \\ u^r &= \frac{1}{f^2 - \omega^2}\left(\left[i\omega\frac{\partial}{\partial \rho} - im\frac{f}{\rho}\right] p - i\omega R + f\Phi\right). \end{aligned} \tag{12}$$

The lateral currents can either be caused by the volume forces directly or they can be driven by the pressure gradient.

With the assumption of a flat ocean ground, the z-dependence can be separated in equation set (9). We assume solutions in the form

$$\begin{aligned} u^{\varphi}(r,\varphi,z,t) =& u^{\varphi}(r,\varphi,t)F(z) \\ u^{r}(r,\varphi,z,t) =& u^{r}(r,\varphi,t)F(z) \\ p(r,\varphi,z,t) =& p(r,\varphi,t)F(z). \end{aligned} \tag{13}$$

Taking this ansatz into (9) and assuming a constant Brunt-Väisälä frequency, a differential equation for F(z) can be found

$$\frac{d^2}{\mathrm{d}z^2}\frac{1}{N^2}F(z) + \lambda^2 F(z) = 0. \tag{14}$$

Equation (14) combined with boundary conditions at the sea bottom and the surface

$$\begin{aligned} N^2\frac{\mathrm{d}F}{\mathrm{d}z} + \frac{F}{g} =& 0 \qquad \text{at } z = 0, \\ \frac{\mathrm{d}F}{\mathrm{d}z} =& 0 \qquad \text{at } z = -H, \end{aligned} \tag{15}$$

forms and eigenvalue problem (see also Fennel and Lass 1989). A complete set of orthogonal eigenfunctions is the solution to the problem, so the variables are expanded in terms of vertical eigenfunctions $F_n(z)$

$$(u^{\varphi}, u^{r}, p) = \sum_{n=0}^{\infty}(u_n^{\varphi}, u_n^{r}, p_n)F_n(z). \tag{16}$$

Substituting (16) into (9), the result for the vertical velocity is

$$w = -\sum_{n=0}^{\infty} N^{-2}(z)\frac{\mathrm{d}F_n(z)}{\mathrm{d}z} r p_n(\rho,\varphi,t). \tag{17}$$

For a constant Brunt-Väisälä frequency, the eigenvalues are $\lambda_0^2 = (gH)^{-1}$ for the barotropic eigenvalue, and $\lambda_n = \frac{n\pi}{NH}$ for the baroclinic eigenvalues.

2.6 Solving the Differential Equation for the Pressure

Now it is time to solve the pressure equation. The task of decoupling the equation set (5) in Fourier space has already been done in Fennel and Lass 1989 for Cartesian coordinates,

so we just use the result

$$-\lambda_n^2 p_n(\omega) + \frac{(k^2+\kappa^2)}{(\omega^2-f^2)} p_n = \frac{-1}{(\omega^2-f^2)} \left[\left(ik + \frac{\kappa f}{\omega} \right) X_n + \left(i\kappa - \frac{fk}{\omega} \right) Y_n \right] \tag{18}$$

and transform it into cylindrical coordinates. Recalling the expressions for the divergence, the Laplace operator and the rotation in cylindrical coordinates (19), the pressure equation (18) is transformed using the same notation for the velocities and the wind forcing as introduced in (9).

The operators in cylindrical coordinates (e.g. Bronstein et al. 2008) are

$$\begin{aligned} \mathrm{curl}_z(X,Y) &= \left(\frac{1}{\rho}\partial_\rho \rho (X,Y)_\varphi - \frac{1}{\rho}\partial_\varphi (X,Y)_\rho \right) \vec{e_z} \\ \mathrm{div}(X,Y) &= \frac{1}{\rho}\partial_\rho \rho (X,Y)_\rho + \frac{1}{\rho}\partial_\varphi (X,Y)_\varphi + \partial_z (X,Y) \\ \triangle_h p &= \frac{1}{\rho}\partial_\rho \left(\rho \partial_\rho p \right) + \frac{1}{\rho^2}\partial_\varphi^2 p \end{aligned} \tag{19}$$

The transformed pressure equation becomes:

$$\begin{aligned} & \left(-\lambda_n^2 \left(f^2 - \omega^2 \right) + \frac{1}{\rho}\partial_\rho \rho \partial_\rho + \frac{1}{\rho^2}\partial_\varphi^2 \right) \left(-i\omega p_n(\rho,\varphi,\omega) \right) \\ = \; & -i\omega \frac{1}{\rho} \left(\partial_\rho \rho R_n(\rho,\varphi,\omega) + \partial_\varphi \Phi_n(\rho,\varphi,\omega) \right) + \frac{f}{\rho} \left(\partial_\rho \rho \Phi_n(\rho,\varphi,\omega) - \partial_\varphi R_n(\rho,\varphi,\omega) \right) \end{aligned} \tag{20}$$

Now we have one single differential equation for the pressure perturbation p and three equations for u^ρ, u^φ and w in dependence of p. Thus by solving the differential equation for p it is also possible to derive the equations for the currents.

Analogous to the depth coordinate before, a separation ansatz is chosen for the angular dependence.

$$\begin{aligned} p_n(\rho,\varphi,\omega) &= \sum_k \tilde{p}_{n,k}(\rho,\omega) e^{ik\varphi} \\ R_n(\rho,\varphi,\omega) &= \sum_k \tilde{R}_{n,k}(\rho,\omega) e^{ik\varphi} \\ \Phi_n(\rho,\varphi,\omega) &= \sum_k \tilde{\Phi}_{n,k}(\rho,\omega) e^{ik\varphi} \end{aligned} \tag{21}$$

Now the angular derivation becomes simply a product by the natural numbers k. The k's have to be element of the integer numbers due to the physical reason, that the pressure

perturbation field is 2π periodic.

$$\begin{aligned}&\sum_k \left(-\lambda_n^2\left(f^2-\omega^2\right)+\frac{1}{\rho}\partial_\rho\rho\partial_\rho-\frac{k^2}{\rho^2}\right)\left(-i\omega\tilde{p}_{n,k}(\omega,\rho)e^{ik\varphi}\right)\\ =&\sum_k -i\omega\frac{1}{\rho}\left(\partial_\rho\rho\tilde{R}_{n,k}(\rho,\omega)e^{ik\varphi}+\partial_\varphi\tilde{\Phi}_{n,k}(\rho,\omega)e^{ik\varphi}\right)+\frac{f}{\rho}\left(\partial_\rho\rho\tilde{\Phi}_{n,k}(\rho,\omega)e^{ik\varphi}-\partial_\varphi\tilde{R}_{n,k}(\rho,\omega)e^{ik\varphi}\right)\end{aligned} \tag{22}$$

Now it is quite easy to perform the Fourier transformation of the angular variable too. Multiplication by $e^{-im\varphi}$ and integration $\int \mathrm{d}\varphi$ results in a product by $\int e^{in\varphi-im\varphi}\mathrm{d}\varphi=\delta_{nm}$:

$$\begin{aligned}&\sum_k \int_{-\infty}^{\infty}\left(-\lambda_n^2\left(f^2-\omega^2\right)+\frac{1}{\rho}\partial_\rho\rho\partial_\rho-\frac{k^2}{\rho^2}\right)\left(-i\omega\tilde{p}_{n,k}(\omega,\rho)e^{ik\varphi-im\varphi}\right)\mathrm{d}\varphi\\ =&\sum_k \int_{-\infty}^{\infty}\left[-\frac{i\omega}{\rho}\left(\partial_\rho\rho R_{n,k}(\rho,\omega)+ik\Phi_{n,k}(\rho,\omega)\right)e^{ik\varphi-im\varphi}+\frac{f}{\rho}\left(\partial_\rho\rho\Phi_{n,k}(\rho,\omega)-ikR_{n,k}(\rho,\omega)\right)e^{ik\varphi-im\varphi}\right]\mathrm{d}\varphi\end{aligned} \tag{23}$$

Evaluating the Fourier transformation of the angular derivatives and applying the δ-function, the resulting equation is

$$\begin{aligned}&\left(-\lambda_n^2\left(f^2-\omega^2\right)+\frac{1}{\rho}\partial_\rho\rho\partial_\rho-\frac{m^2}{\rho^2}\right)\left(-i\omega\tilde{p}_{n,m}(\omega,\rho)\right)\\ =&-\frac{i\omega}{\rho}\left(\partial_\rho\rho R_{n,m}(\rho,m,\omega)-im\Phi_{n,m}(\rho,\omega)\right)+\frac{f}{\rho}\left(\partial_\rho\rho\Phi_{n,m}(\rho,\omega)+imR_{n,m}(\rho,\omega)\right).\end{aligned} \tag{24}$$

This is the Helmholtz differential equation. A substitution of ρ leads (depending on the sign) either to the ordinary Bessel differential equation or to the modified Bessel differential equation.

ordinary Bessel diff. equation	**modified Bessel diff. equation**
$r=\lambda_n\sqrt{\omega^2-f^2}\rho\rightarrow\rho=\frac{r}{\lambda_n\sqrt{\omega^2-f^2}}$	$r=\lambda_n\sqrt{f^2-\omega^2}\rho\rightarrow\rho=\frac{r}{\lambda\sqrt{f^2-\omega^2}}$
for the case $\omega\gg f$	for the case $\omega\ll f$

We will keep in mind, that also the r depends on the vertical modes, but drop the index n for better readability. The case differentiation shown in the table is of importance for the solutions considered later on. The comparison of ω with the Coriolis frequency f is going to determine the sign in the Bessel differential equation (28). The ordinary Bessel differential equation is describing processes, which are fast in comparison to the Coriolis frequency, the modified Bessel differential equation is describing slower processes.

Dropping the explicit notation of the dependencies for now ($R_n = R_n(\rho,m,\omega)$, $\Phi_n = \Phi_n(\rho,m,\omega)$) the equation can be written in a shorter way. With the substitution that leads to the normal Bessel differential equation:

$$\begin{aligned}&\left(\lambda_n^2(\omega^2-f^2)\frac{\partial^2}{\partial r^2}+\lambda_n^2(\omega^2-f^2)\frac{1}{r}\frac{\partial}{\partial r}+\left(-\lambda_n^2(f^2-\omega^2)-\lambda_n^2(\omega^2-f^2)\frac{m^2}{r^2}\right)\right)(-i\omega\tilde{p}_{n,m}(\omega,\rho))\\ =&\frac{1}{2\pi}\frac{\lambda_n\sqrt{\omega^2-f^2}}{r}\left[-i\omega\left(\partial_r rR_{n,m}-imR_{n,m}\right)+f\left(\partial_r r\Phi_{n,m}+imR_{n,m}\right)\right]\end{aligned} \tag{25}$$

$$\begin{aligned}&\left(\frac{\partial^2}{\partial r^2}+\frac{1}{r}\frac{\partial}{\partial r}+\left(+1-\frac{m^2}{r^2}\right)\right)(\tilde{p}_{n,m}(\omega,\rho))\\ =&\underbrace{-\frac{1}{2\pi i\omega}\frac{1}{r\lambda_n\sqrt{\omega^2-f^2}}\left[-i\omega\left(\partial_r rR_{n,m}-imR_{n,m}\right)+f\left(\partial_r r\Phi_{n,m}+imR_{n,m}\right)\right]}_{F_{n,m}(r,\omega,m)/r\text{ (Inhomogeneity ordinary Bessel function)}}\end{aligned} \tag{26}$$

And with the second substitution which leads to the modified Bessel differential equation

$$\begin{aligned}&\left(\frac{\partial^2}{\partial r^2}+\frac{1}{r}\frac{\partial}{\partial r}+\left(-1-\frac{m^2}{r^2}\right)\right)(\tilde{p}_{n,m}(\omega,\rho))\\ =&\underbrace{-\frac{1}{2\pi i\omega}\frac{1}{r\lambda_n\sqrt{f^2-\omega^2}}\left[-i\omega\left(\partial_r rR_{n,m}-imR_{n,m}\right)+f\left(\partial_r r\Phi_{n,m}+imR_{n,m}\right)\right]}_{F_{n,m}(r,\omega,m)/r\text{ (Inhomogeneity modified Bessel function)}}.\end{aligned} \tag{27}$$

2.6.1 Derivation of the Greens Function

With the abbreviation for the inhomogeneity indicated above and by omitting the indexes m and n for now, the differential equation becomes:

$$r'\left(\frac{\partial^2}{\partial r'^2}+\frac{1}{r'}\frac{\partial}{\partial r'}+\left(\pm1-\frac{m^2}{r'^2}\right)\right)p(r')=F(r') \tag{28}$$

The plus and the minus sign are determining the ordinary/modified Bessel differential equation respectively. A formal solution for (28) can be derived with the method of the Green's function. The defining equation for the Green's function is

$$r'\frac{\partial^2}{\partial r'^2}G(r,r')+\frac{\partial}{\partial r'}G(r,r')+r'\left(\pm1-\frac{m^2}{r'^2}\right)G(r,r')=\delta(r-r'). \tag{29}$$

A multiplication of (28) from the left side with $r'G(r,r')$ delivers (30). Multiplication of (30) with $p(r',\varphi)$ becomes (31).

$$G(r,r')r'\frac{\partial^2}{\partial r'^2}p(r',\varphi')+G(r,r')\frac{\partial}{\partial r'}p(r')+G(r,r')r'\left(\pm1-\frac{m^2}{r'^2}\right)p(r',\varphi')=G(r,r')r'F(r',\varphi) \tag{30}$$

$$p(r',\varphi')r'\frac{\partial^2}{\partial r'^2}G(r,r')+p(r',\varphi)\frac{\partial}{\partial r'}G(r,r')+p(r',\varphi)r'\left(\pm1-\frac{m^2}{r'^2}\right)G(r,r')=\delta(r-r')p(r',\varphi) \tag{31}$$

Integrating over $\int_0^\infty f(r,r')dr'$ and then subtracting both equations from each other gives

$$\begin{aligned} p(r,\varphi)=&\int_0^\infty r'G(r,r')F(r',\varphi)dr'+\int_0^\infty\left(r'p(r')\frac{\partial^2}{\partial r'^2}G(r,r')-r'G(r,r')\frac{\partial^2}{\partial r'^2}p(r')\right)dr' \\ &+\int_0^\infty\left(p(r')\frac{\partial}{\partial r'}G(r,r')-G(r,r')\frac{\partial}{\partial r'}p(r')\right)dr' \end{aligned} \tag{32}$$

To avoid lengthyness, a shorter notation for the convolution is introduced

$$G\star X=\int_0^\infty G(r,r')F(r',\varphi)\mathrm{d}r' \quad\text{and}\quad G\star r'X=\int_0^\infty r'G(r,r')F(r',\varphi)\mathrm{d}r'. \tag{33}$$

By integrating the first term with the r' derivatives partially, we gain

$$\begin{aligned} p(r)=&G\star r'F+\int_0^\infty\left(r'p(r')\frac{\partial^2}{\partial r'^2}G(r,r')-r'G(r,r')\frac{\partial^2}{\partial r'^2}p(r')\right)dr' \\ &+\int_0^\infty\left(p(r')\frac{\partial}{\partial r'}G(r,r')-G(r,r')\frac{\partial}{\partial r'}p(r')\right)dr' \\ =&G\star r'F+\left[r'p(r')\frac{\partial}{\partial r'}G(r,r')\right]_0^\infty-\left[r'G(r,r')\frac{\partial}{\partial r'}p(r')\right]_0^\infty. \end{aligned} \tag{34}$$

Now it is easy to see the necessary boundary conditions for the Greens function

- for $r'\to0$, the $p(r')$,$G(r,r')$, $\frac{\partial}{\partial r'}p(r')$ and $\frac{\partial}{\partial r'}G(r,r')$ may not diverge faster than 1/r.
- for $r'\to\infty$, the $p(r')\frac{\partial}{\partial r'}G(r,r')$ and $G(r,r')\frac{\partial}{\partial r'}p(r')$ have to approach zero faster then linearly.

The boundary conditions of the Greens function for the ordinary- and the modified Bessel differential equations are the same.

Returning to equation (31), but this time not multiplied by pr' but by r'^2, the result is the Bessel differential equation in its ordinary form.

$$\left(r'^2\frac{\partial^2}{\partial r'^2}G(r,r') + r'\frac{\partial}{\partial r'}G(r,r') + G(r,r')\left(\pm r'^2 - m^2\right)\right) = r'\delta(r-r'). \tag{35}$$

The solutions of the homogeneous Bessel differential equation are the Bessel functions J_m, Y_m and the Hankel functions $H^{(1)}, H^{(2)}$ for the positive sign. For the negative sign, thus for the modified Bessel differential equation, the solutions are the Bessel functions I_m, K_m (Abramowitz and Stegun 1972).

For the Greens function, the ansatz $G(r,r') = \theta(r-r')g^{>}(r,r') + \theta(r'-r)g^{<}(r,r')$ is used in equation (35). Using the boundary conditions derived above, we arrive finally at the complete Greens function for the ordinary Bessel differential equation

$$G(r,r') = \frac{\pi}{2}\left(\theta(r-r')J_m(r')Y_m(r) + \theta(r'-r)Y_m(r')J_m(r)\right) \tag{36}$$

and the modified Bessel differential equation respectively

$$G(r,r') = \theta(r-r')I_m(r')K_m(r) + \theta(r'-r)K_m(r')I_m(r) \tag{37}$$

The Greens function already shows the basic features of the solution for specific wind fields (section 2.7).The Greens function is consistent of two parts. The first one is describing the behaviour in the inner, wind influenced area ($\theta(r_0 - r)$). The second one is describing the behaviour outside of it ($\theta(r - r_0)$). Inside of the wind influenced area, components of the pressure perturbation are proportional to the class of Bessel functions I_m, that are growing exponentially with the distance. Outside, the class of functions K_m takes over. It decreases exponentially.

2.7 Application of the Theory to Different Wind Fields

In the previous chapter, a formal solution to the differential equation describing the wind driven pressure perturbation was derived. This formal solution is not easy to analyze yet, and the specific solutions for different wind fields are not obvious. There is some more work to be done in order to get a realistic picture of currents, that are driven by different wind fields.

2.7.1 Wind Fields of Interest

Recall, that the aim of this work is to model a simple ecosystem within an upwelling area. The formal solution of the Boussinesq equations has been derived in polar coordinates to

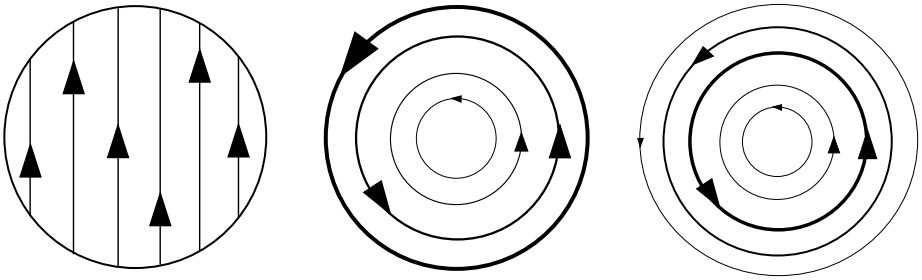

(i) (ii) (iii)

Figure 1: *Three different wind fields. The picture shows a scheme of the distribution of the wind stress on the water. The respective formulas describing this fields and the currents they cause can be found in the subsections 2.7.2, 2.7.3 and 2.7.4.*

allow an easy description of wind fields with a rotational structure. Upwelling currents establish in steady state under rotational wind forcings on wind edges.
To archive a base for the advection in the ecosystem model to come, the formal solution is employed on different wind fields giving an impression of the resulting currents under the influence of rotational wind stress. The focus in this work are processes with a time scale much longer than the inertial oscillations ($\omega \ll f$), thus the formal solution for the modified Bessel differential equation is employed.
Three exemplaric wind fields (see also fig. 1) are chosen for this task, they are causing interesting vertical velocity profiles and are easy enough in their mathematical structure to allow an analytic inverse Fourier transformation.

2.7.2 Circular Wind Patch

The first wind field to apply the formal solution to is a round wind patch with a homogeneous linear wind inside (see fig. 1i). This wind field has a divergence at the front and the back side. At the wind edges on the right and the left side, it causes a rotational wind stress. The curl is mathematically positive at the left hand side and negative at the right hand side. The wind edges are realized with the help of the Theta-function, causing the wind to decrease in a sharp wind edge at the radius ρ_0.

$$\begin{aligned} \Phi(\varphi, z, t) &= \frac{u_*^2}{H_{mix}} \theta\left(z + H_{mix}\right) \theta\left(\rho_0 - \rho\right) \theta(t) \cos(\varphi) \\ R(\varphi, z, t) &= \frac{u_*^2}{H_{mix}} \theta\left(z + H_{mix}\right) \theta\left(\rho_0 - \rho\right) \theta(t) \sin(\varphi) \end{aligned} \tag{38}$$

The parameter u_*^2 is defined as $u_*^2 = \frac{\tau}{\rho_0} = \frac{\rho_a}{\rho_0} c_{10} W_{10}^{(x,y)} W_{10}$ (Fennel and Lass 1989, p22).

c_{10} is the drag coefficient in the order of 10^{-3}, W_{10} is the wind velocity ten meters over the sea surface. ρ_a and ρ_o is the density of the air and seawater respectively. So for a wind velocity of $10\frac{m}{s}$, u_* is round about $0.01\frac{m}{s}$.
The Fourier transformation according to (11) and (21) in the angular coordinate φ, the time t and the separation into vertical modes gives:

$$\begin{aligned}\Phi_{n,m}(m,\omega) =& \frac{u_*^2}{h_n}\theta\left(r_0 - r'\right)\frac{i}{\omega + i\epsilon}\pi\left(\delta_{m,-1} + \delta_{m,1}\right)\\ R_{n,m}(m,\omega) =& \frac{u_*^2}{h_n}\theta\left(r_0 - r'\right)\frac{i}{\omega + i\epsilon}\frac{\pi}{i}\left(\delta_{m,-1} - \delta_{m,1}\right)\end{aligned} \tag{39}$$

To get the pressure perturbation, the formal solution is applied to the transformed wind field and the integrals and the sum has to be computed. The whole calculation is to be found in the annex.

$$\begin{aligned}p_n(r,\varphi,t) &= \int_{-\infty}^{\infty}\int_0^{\infty}\sum_{m=-\infty}^{\infty} r' G_m(r,r') F(r',\varphi,\omega) e^{im\varphi - i\omega t}\mathrm{d}r'\mathrm{d}\omega\\ &= \theta(t)\frac{u_*^2}{h_n}\rho_0\left[\theta(\rho-\rho_0)I_1(\lambda_n f\rho_0)K_1(\lambda_n f\rho) + \theta(\rho_0-\rho)K_1(\lambda_n f\rho_0)I_1(\lambda_n f\rho)\right]\Big[\sin(\varphi) - tf\cos(\varphi)\Big]\end{aligned} \tag{40}$$

Not surprisingly, the solution for p_n shows different features inside of the wind influenced area $\theta(\rho_0 - \rho)$ and outside of it. One of the terms is constant in time and one is linearly growing. The constant term can be located at the parts with the strongest wind divergence. The linearly growing pressure perturbation is caused by the rotational wind stress at the wind edges.
The vertical velocity can be derived simply by taking the time derivative of the pressure perturbation (see eq. 9) or (Fennel and Lass 1989, 3.8.13).

$$w_n(r,\varphi,t) = -\theta(t)\frac{u_*^2}{h_n}\rho_0\left[\theta(\rho-\rho_0)I_1(\lambda_n f\rho_0)K_1(\lambda_n f\rho) + \theta(\rho_0-\rho)K_1(\lambda_n f\rho_0)I_1(\lambda_n f\rho)\right]\Big[f\cos(\varphi)\Big] \tag{41}$$

In equation 41, we can see different features on the right and the left wind edge. There is constant positive upwelling at the wind edge with positive wind stress curl on the left wind edge (for positive f on the northern hemisphere), and downwelling on the right wind edge.

To derive the velocities u_n^r and u_n^φ the equation set (12) is used and for a more readable notation, two abbreviations are introduced:

$$A_n = \left[\theta(\rho-\rho_0)I_1(\lambda_n f\rho_0)K_1(\lambda_n f\rho) + \theta(\rho_0-\rho)K_1(\lambda_n f\rho_0)I_1(\lambda_n f\rho)\right]$$

$$B_n = \left[-\theta(\rho-\rho_0)I_1(\lambda_n f\rho_0)K_0(\lambda_n f\rho) + \theta(\rho_0-\rho)K_1(\lambda_n f\rho_0)I_0(\lambda_n f\rho)\right]$$

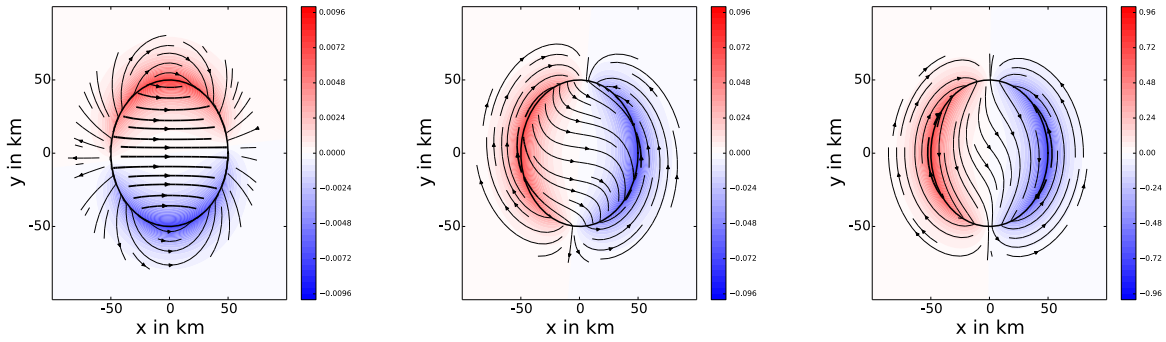

Figure 2: *pressure perturbation and horizontal velocities of the first baroclinic mode. In the start, pressure perturbations are visible at the upper and lower wind edges were wind divergence is largest. Later it is overlayed by the linearly increasing pressure perturbation at the sides of the wind field. The arrows in the diagram mark the horizontal velocity. After the onset of the wind, an Ekman transport establishes which is then covered by the strong pressure perturbations forcing the water masses flowing against the wind forcing*

Angular velocity

The result of the pressure equation is inserted into (12). For the inverse Fourier transformation, $w \ll f$ is taken into account again, thus assuming $f^2 - \omega^2 \approx f^2$.

$$\begin{aligned} u_n^{\varphi} =& \frac{1}{f}\left(\frac{\partial}{\partial\rho}p_n - R_n\right) \\ =& -\frac{1}{f^2}\frac{u_*^2}{h_n}\left(\frac{\rho_0}{\rho}A_n(\rho)\theta(t)f\sin(\varphi)\right) \\ &+ \frac{1}{f}\frac{u_*^2}{h_n}\theta(t)\rho_0\Big[\frac{1}{R_n}\,B_n(\rho) - \frac{1}{\rho}A_n(\rho)\Big]\Big[\sin(\varphi) - tf\cos(\varphi)\Big] \\ &- \frac{1}{f}\frac{u_*^2}{h_n}\theta(t)\theta\left(\rho_0 - \rho\right)\sin(\varphi) \end{aligned} \tag{42}$$

The angular velocity can basically be separated into two parts. The sinus terms are the currents, which run perpendicular to the wind stress. They are constant in time and can be interpreted as the Ekman transport processes.

The cosine terms are the velocity components, which run in parallel to the wind stress. This part is growing linearly in time.

radial velocity

$$
\begin{aligned}
u_n^\rho &= \frac{1}{f}\left(\Phi_n - \frac{1}{\rho}\frac{\partial}{\partial\varphi}p_n\right) \\
&= -\frac{1}{f^2}\frac{u_*^2}{h_n}\left(\rho_0\Big[\frac{1}{R_n}B_n(\rho) - \frac{1}{\rho}A_n(\rho)\Big]\Big[-\theta(t)f\cos(\varphi)\Big]\right) \\
&+ \frac{1}{f}\frac{u_*^2}{h_n}\theta(t)\theta\left(\rho_0-\rho\right)\cos(\varphi) \\
&- \frac{1}{f}\frac{u_*^2}{h_n}\theta(t)\frac{\rho_0}{\rho}A_n(\rho)\left[\cos(\varphi) + tf\sin(\varphi)\right]
\end{aligned}
\tag{43}
$$

The result for the radial velocity looks similar to the result obtained for the angular velocity. Mostly the cosines and sines are exchanged, so the highest radial velocity is at the top and bottom side of the wind field, in parallel to the wind stress.

The rotation $\mathrm{curl}_z(\tau)$ of wind stress is strongest at the wind edges. It is mathematically positive (counter clockwise) at the left side and negative at the right side. Perturbations with opposite sign can be seen on the left and the right side of the wind field. This perturbations are resulting in a downwelling current at the right wind edge and an upwelling current at the left wind edge. The pressure profile shows a maximum perturbation at $r = r_0$, resulting in vertical current at $r = r_0$ with a maximum velocity at $z = -H_{mix}$. There are no counter currents beyond the wind edges as seen for the other examples. The continuity equation does not require these currents to be fulfilled in this example, the water masses are following a closed circular motion already. The water is upwelled at the left wind edge, and then flowing (positive u) to the right wind edge. Here it is downwelled again and returning by a negative u current under the mixed layer to its origin.

The currents fulfill the continuity equation $\frac{\partial}{\partial\rho}u_n^\rho + \frac{u_n^\rho}{\rho} + \frac{1}{\rho}\frac{\partial u_n^\varphi}{\partial\varphi} + \lambda_n^2\frac{\partial}{\partial t}p_n = 0$.

2.7.3 Rotational, Linear Increasing Wind Field

The next examplaric wind field is a pure rotational wind. The wind stress is defined by

$$
\begin{aligned}
\Phi(\rho',\varphi,z,t) &= \frac{u_*^2}{H_{mix}}\rho'\theta\left(z+H_{mix}\right)\theta\left(\rho_0-\rho'\right)\theta(t) \\
R(\rho',\varphi,z,t) &= 0.
\end{aligned}
\tag{44}
$$

Pressure perturbation and currents driven by the wind patch

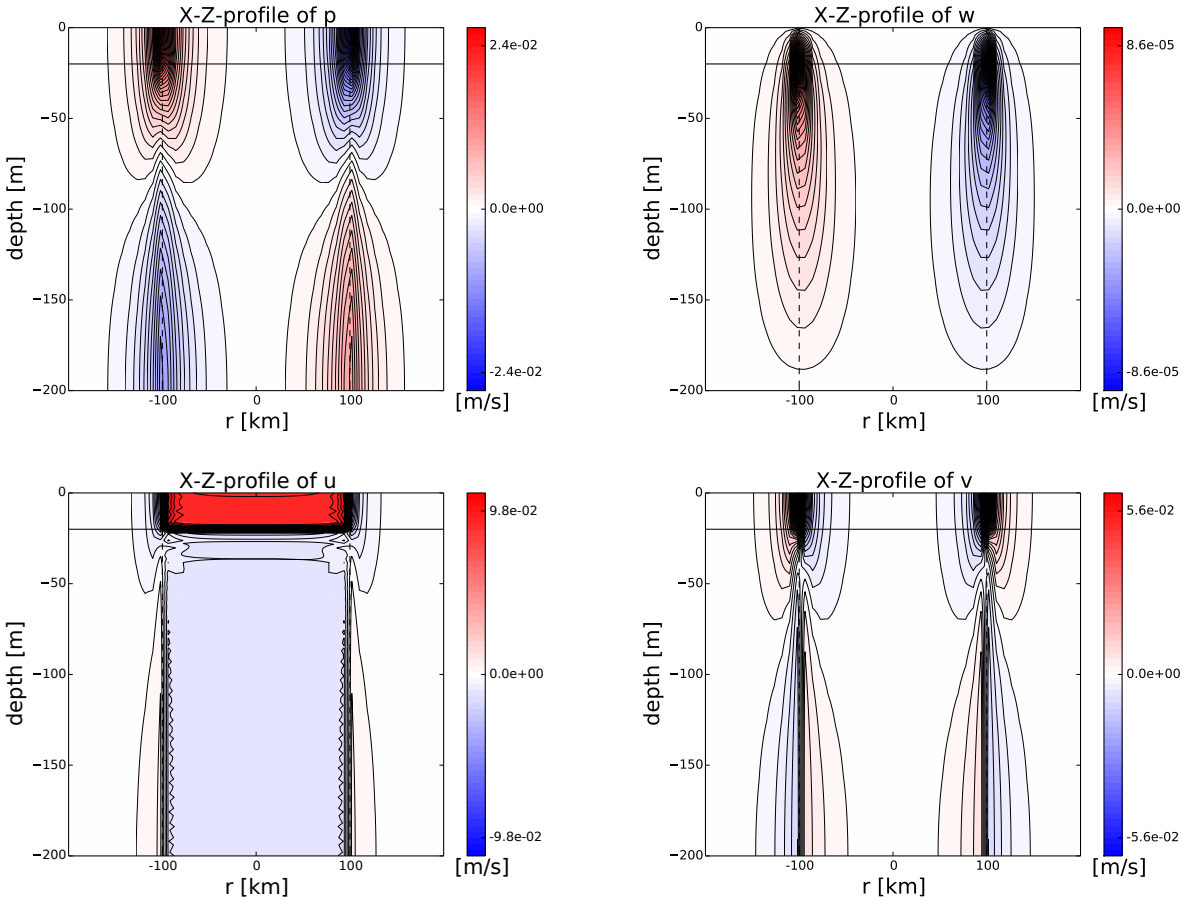

Figure 3: *Resulting pressure perturbation and currents driven by the homogeneous wind field from section 2.7.2. This plots are done taking the mode sum of the resulting equations. The parameters for this plot are* $t = 10\text{h}$, *radius of wind field* $r = 50\text{km}$, $H_{mix} = 20m$, $H = 200m$, *constant BVF,* $f = 5 \cdot 10^{-5}\text{s}^{-1}$, *and* $u^* = 0.01m/s$.

For a schematic drawing, see (fig. 1ii). It is polar symmetric. The Fourier transformation and decomposition into vertical modes of the angular part of the wind stress is

$$\begin{aligned}\Phi_{n,m}(r',m,\omega) =& 2\pi\delta_{m,0}\frac{u_*^2}{h_n}\rho'\frac{i}{\omega+i\epsilon}\theta\left(r_0-r'\right)\\ R_{n,m}(r',m,\omega) =& 0.\end{aligned} \tag{45}$$

As the main interest of this work is focused at processes with $\omega \ll f$, the formal solution for the modified Bessel differential equation is employed. Applying the formal solution to the wind fields, after taking the sum over all m's, the result for the pressure is

$$\begin{aligned}p_n(r,\varphi) =& \int_0^\infty r' G(r,r') F(r',\varphi) dr'\\ =& -\frac{f}{\lambda_n\sqrt{f^2-\omega^2}}\frac{u_*^2}{h_n}\frac{i}{(\omega+i\epsilon)^2}\int_0^\infty G(r,r')\left[\left(\frac{\partial_{r'}r'^2}{\lambda_n\sqrt{f^2-\omega^2}}\theta\left(r_0-r'\right)\right)\right]dr'\\ =& \underbrace{\frac{f}{\lambda_n^2\left(f^2-\omega^2\right)}\frac{u_*^2}{h_n}\frac{-1}{\left(\omega+i\epsilon\right)^2}}_{\gamma_2}\int_0^\infty G(r,r')\left[2r'\theta\left(r_0-r'\right)-r'^2\delta\left(r_0-r'\right)\right]dr'\end{aligned} \tag{46}$$

The integration over r has to be done piecewise for $r < r_0$ and $r > r_0$.

$$G\star r'\theta(r-r') = \theta(r-r_0)\int_0^{r_0} dr' r' G^{>}(r,r') + \theta(r_0-r)\left[\int_0^{r} dr' r' G^{>}(r,r') + \int_r^{r_0} dr' r' G^{<}(r,r')\right] \tag{47}$$

For the integrals over the different Bessel functions, the integrals from section (7.1) are used.

$$\begin{aligned}p_n(r,\varphi,\omega) =& \gamma_2\int_0^\infty G(r,r')\left[2r'\theta\left(r_0-r'\right)-r'^2\delta\left(r_0-r'\right)\right]dr'\\ =& \gamma_2\theta(r-r_0)\left[2-r_0^2 I_0(r)\left(\frac{2}{r_0}K_1(r_0)-K_0(r_0)\right)\right]\\ &+\gamma_2\theta(r_0-r)\left[r_0^2 K_0(r)\left(\frac{2}{r_0}I_1(r_0)-I_0(r_0)\right)\right]\end{aligned} \tag{48}$$

If the inverse Fourier transformation is done using the approximation $\omega \ll f$, the equation

for the pressure perturbation becomes

$$p_n(\rho,\varphi,t) = \frac{\theta(t)tu_*^2}{\lambda_n h_n}\left(\theta(\lambda_n f\rho - \lambda_n f\rho_0)\left[2-(\lambda_n f\rho_0)^2 I_0(\lambda_n f\rho)\left(\frac{2}{\lambda_n f\rho_0}K_1(\lambda_n f\rho_0)-K_0(\lambda_n f\rho_0)\right)\right]\right.$$
$$\left.+\theta(\lambda_n f\rho_0 - \lambda_n f\rho)\left[(\lambda_n f\rho_0)^2 K_0(\lambda_n f\rho)\left(\frac{2}{\lambda_n f\rho_0}I_1(\lambda_n f\rho_0)-I_0(\lambda_n f\rho_0)\right)\right]\right) \tag{49}$$

The **vertical velocity** is:

$$\begin{aligned} w_n =& \frac{\partial}{\partial t}p_n \\ =& \frac{\theta(t)u_*^2}{\lambda_n h_n}\left(\theta(\lambda_n f\rho - \lambda_n f\rho_0)\left[2-(\lambda_n f\rho_0)^2 I_0(r)\left(\frac{2}{\lambda_n f\rho_0}K_1(\lambda_n f\rho_0)-K_0(\lambda_n f\rho_0)\right)\right]\right. \\ &\left.+\gamma_2\theta(\lambda_n f\rho_0 - \lambda_n f\rho)\left[(\lambda_n f\rho_0)^2 K_0(\lambda_n f\rho)\left(\frac{2}{\lambda_n f\rho_0}I_1(\lambda_n f\rho_0)-I_0(\lambda_n f\rho_0)\right)\right]\right) \end{aligned} \tag{50}$$

angular velocity:

$$\begin{aligned} u_n^\varphi =& \frac{\theta(t)tu_*^2}{h_n}\theta(\lambda_n f\rho - \lambda_n f\rho_0)\left[(\lambda_n f\rho_0)^2 I_1(\lambda_n f\rho)\left(\frac{2}{\lambda_n f\rho_0}K_1(\lambda_n f\rho_0)-K_0(\lambda_n f\rho_0)\right)\right] \\ &-\frac{\theta(t)tu_*^2}{h_n}\theta(\lambda_n f\rho_0 - \lambda_n f\rho)\left[(\lambda_n f\rho_0)^2 K_1(\lambda_n f\rho)\left(\frac{2}{\lambda_n f\rho_0}I_1(\lambda_n f\rho_0)-I_0(\lambda_n f\rho_0)\right)\right] \end{aligned} \tag{51}$$

radial velocity:

$$\begin{aligned} u_n^\rho =& \frac{\theta(t)u_*^2}{fh_n}\theta(\lambda_n f\rho - \lambda_n f\rho_0)\left[(\lambda_n f\rho_0)^2\lambda_n f I_1(\lambda_n f\rho)\left(\frac{2}{\lambda_n f\rho_0}K_1(\lambda_n f\rho_0)-K_0(\lambda_n f\rho_0)\right)\right] \\ &-\frac{\theta(t)u_*^2}{fh_n}\theta(\lambda_n f\rho_0 - \lambda_n f\rho)\left[(\lambda_n f\rho_0)^2 K_1(\lambda_n f\rho)\left(\frac{2}{\lambda_n f\rho_0}I_1(\lambda_n f\rho_0)-I_0(\lambda_n f\rho_0)\right)\right] \\ &+\frac{1}{f}\frac{u_*^2}{h_n}\lambda_n f\rho\theta(\lambda_n f\rho_0 - \lambda_n f\rho)\theta(t) \end{aligned} \tag{52}$$

The pressure perturbation and the currents show no dependency on φ, they are polar symmetric.

The rotation, $\mathrm{curl}_z(\tau)$, of the wind stress is constant and positive within r, thus resulting in an upwelling current on the northern hemisphere. The pressure profile shows a maximum perturbation at $r = 0$ and $z = -H_{mix}$, decreasing to the wind edges where it becomes zero. At the sides of the wind field is an opposite pressure perturbation located, that

is causing a downwelling current. The upwelled water is leaving the wind influenced area in the mixed layer to the sides (red colour in the radial velocity profile). A current directed into the opposite direction is located under the mixed layer, bringing water into the system (negative radial velocity). The wind driven water masses are undergoing a circular motion in an otherwise undisturbed ocean.
The whole water body starts to rotate in the wind influenced area, a geostrophic balance establishes. There are no friction forces considered, therefore the radial velocities reach unrealistic high values in this model. In reality the pressure perturbation cannot grow unlimited over time but would be decreased by turbulent downmixing of the pycnocline. The rotational motion could also be limited by shear friction with the surrounding water masses and bottom friction.

Neither the radial velocity nor the angular velocity are depended on φ. The continuity equation (12.3) is only balanced by the vertical velocity w and the radial velocity u^r. The angular derivative of the angular velocity is vanishing.

2.7.4 Rotational Wind Forcing with r·exp(-r)-shape

So far only wind fields with a very simplified structure and hard wind edges were considered. The next example uses a more realistic, rotational wind field. This a continuous rotational wind field without any wind edges at the sides. It is defined in the following mathematical form

$$\begin{aligned} \phi(r,\varphi,z,t) =& \frac{u_*^2}{H_{mix}}\theta\left(z+H_{mix}\right) r e^{-r}\theta(t) \\ R(r,\varphi,z,t) =& 0. \end{aligned} \tag{53}$$

The Fourier transformation and separation into vertical modes gives

$$\begin{aligned} \phi_{n,m}(r,m,\omega) =& \frac{u_*^2}{h_n}\frac{2i}{\omega}\pi\delta_{m,0} r e^{-r} \\ R_{n,m}(r,m,\omega) =& 0 \end{aligned} \tag{54}$$

The resulting pressure perturbation looks different from the one for linear increasing wind in section 2.7.3. Due to the lack of wind edges, the solution is not separated into areas by the theta function any longer.

Pressure perturbation and currents driven by rotational (second) wind field

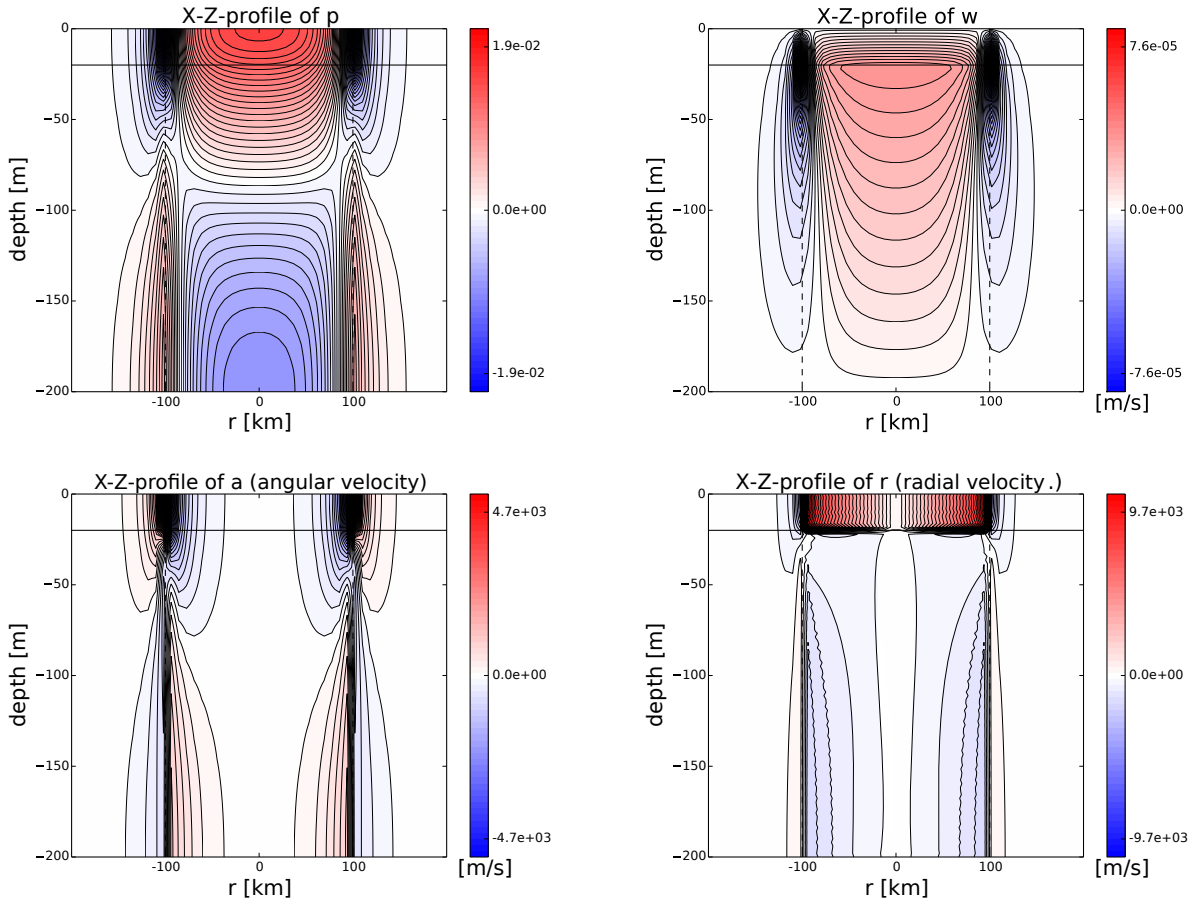

Figure 4: *Resulting pressure perturbation and currents driven by the linearly increasing wind field in section 2.7.3. These plots are done taking the mode sum of the resulting equations in section (2.7.3). The parameters are* $t = 10\text{h}$*, radius of wind field* $r = 50\text{km}$*,* $H_{mix} = 20m$*,* $H = 200m$*, constant BVF,* $f = 5 \cdot 10^{-5}\text{s}^{-1}$*, and* $u^* = 0.01m/s$*.*

$$
\begin{aligned}
p_n(r,\varphi,t) &= \int_{-\infty}^{\infty} \mathrm{d}\omega\gamma \int_0^{\infty} \mathrm{d}r' \Sigma_{-\infty}^{\infty} G_m(r,r') \left(f \frac{\partial}{\partial r} r' \phi_n \right) e^{im\varphi - i\omega t} \\
&= \frac{u_*^2}{h_n} \frac{1}{\lambda_n} \theta(t) t \frac{1}{15} e^{-r} \left(3r^2 - 6r - 6 \right) \\
p_n(\rho,\varphi,t) &= \frac{u_*^2}{h_n} \frac{1}{\lambda_n} \theta(t) t \frac{1}{15} e^{-\lambda_n f \rho} \left(3(\lambda_n f \rho)^2 - 6\lambda_n f \rho - 6 \right)
\end{aligned}
$$

Instead an anti exponential function multiplied with a simple polynomial in ρ is the equation for the whole area. The whole pressure perturbation is growing linearly with

time, just like before in the case of the radially growing wind field. The in depth structure looks more complicated now than before. This can be due to the different forcing of the modes.

The modal **vertical velocity** is the time derivative of the modal pressure perturbation

$$w_n(\rho,\varphi,t) = \frac{u_*^2}{h_n}\frac{1}{\lambda_n}\theta(t)\frac{1}{15}e^{-\lambda_n f\rho}\left(3(\lambda_n f\rho)^2 - 6\lambda_n f\rho - 6\right) \tag{55}$$

The **radial velocity** is constant in time. The contineous wind forcing also leads to contineous velocity profiles.

$$\begin{aligned} u_n^\rho =& -\frac{1}{f^2}\frac{\partial}{\partial t}\left(\frac{\partial}{\partial\rho}p_n\right) + \frac{1}{f}\phi_n \\ =& -\frac{u_*^2}{h_n}\frac{1}{f}\theta(t)\frac{1}{15}e^{-\lambda_n f\rho}\left(-3(\lambda_n f\rho)^2 + 12\lambda_n f\rho\right) + \frac{u_*^2}{h_n}\frac{1}{f}\theta(t)\lambda_n f\rho e^{-\lambda_n f\rho} \\ =& \frac{u_*^2}{h_n}\frac{\lambda_n f\rho}{f}\theta(t)\frac{1}{15}e^{-\lambda_n f\rho}\left(3\lambda_n f\rho + 3\right) \end{aligned} \tag{56}$$

The **angular velocity** is, like in the rotational wind field before, linearly growing in time.

$$\begin{aligned} u_n^\varphi =& \frac{1}{f}\left(\frac{\partial}{\partial\rho}p_n - R_n\right) \\ =& \frac{u_*^2}{h_n}\theta(t)t\frac{1}{15}e^{-\lambda_n f\rho}\left(-3(\lambda_n f\rho)^2 + 12\lambda_n f\rho\right) \end{aligned} \tag{57}$$

The rotation, $\mathrm{curl}_z(\tau)$, of the wind stress has its maximum around $\rho = 0$ and is positive within r, thus resulting in an upwelling current on the northern hemisphere. The pressure profile shows a maximum perturbation in the middle of the wind field at the bottom and the surface of the water column and is decreasing to the sides. The currents have similar features as the ones already seen in section 2.7.2. Water is entering the wind influenced area under the mixed layer, is getting upwelled under the influence of the wind and leaves the area in the mixed layer.

Still the profiles for the continuous wind field look substantially different from the ones before. The dotted lines loose their meaning (as a wind edge) in a continuous wind field and are just included for orientation and comparison to the other wind fields. In comparison to the upwelling current in section 2.7.2, the upwelling is concentrated near the origin here. The corresponding downwelling happens far away from the coordinate origin in this case.

Corresponding to the upwelling in the middle, there is again an outward directed current

visible in the r-profile. Like for the wind field before in section (2.7.3), the currents fields are polar symmetric and the water mass starts to rotate.

Pressure perturbation and currents driven by the continuous wind field

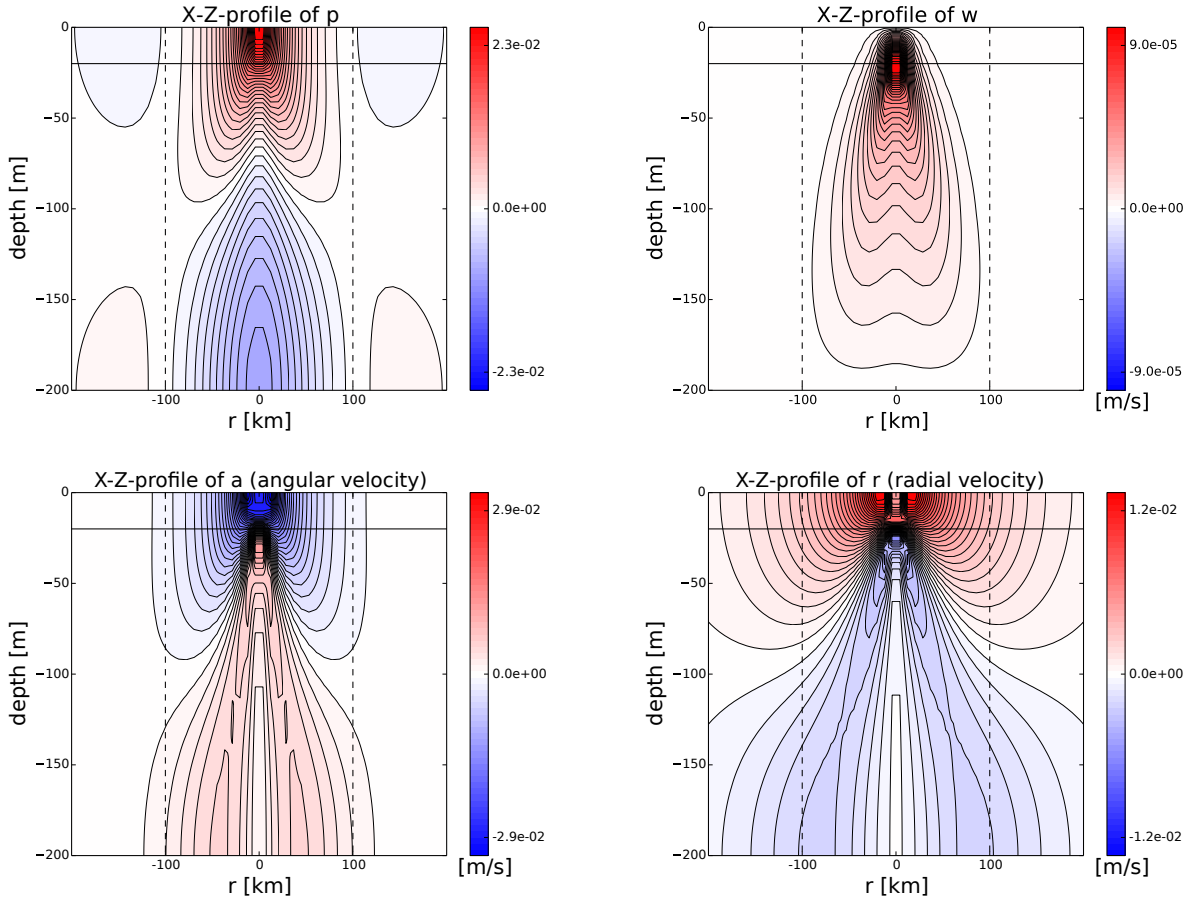

Figure 5: *Resulting pressure perturbation and currents driven by the third (continuous) wind field. These plots are created by taking the mode sum of the resulting current equations in section (2.7.4). The parameters are* $t = 10\text{h}$, *radius of wind field* $r = 50\text{km}$, $H_{mix} = 20m$, $H = 200m$, *constant BVF,* $f = 5 \cdot 10^{-5}\text{s}^{-1}$, *and* $u^* = 0.01m/s$.

3 Ecosystem Model

The physical circulation model in the previous chapter resulted in physical equations, describing the circulation of the seawater in and around an upwelling area. These equations are forming an important base for the description and modelling of an ecosystem within an upwelling area.

The aim of the ecosystem model is to be able to take forth simple analytical equations describing basic biological processes and properties in the 3D-circulation model.

The components of the system will basically be described as tracers in the water, following the currents of the physical model. The model is a biomass model, not considering the motion of individuals.

3.1 Table of Variables and Abbreviations for the Ecosystem Model

In order to keep the terms in the following derivations short and readable, a set of abbreviations is used. A table of variables and abbreviations is given here.

symbol	**meaning**
z	depth coordinate [m]
φ	angular coordinate
ρ	radial coordinate [m]
R	radius of the system [m]
w_e	maximum vertical velocity [m/s]
w_s	sinking velocity of the detritus (negative) [m/s]
A_v	diffusion constant [m^2/s]
H	depth of the ocean (positive)[m]
H_{mix}	depth of the mixed layer (positive)[m]
l_d	rate constant [1/s]
T_b^o	bottom layer tracer concentration at boundaries of system [mol/kg]
$T_b^i(z)$	bottom layer tracer concentration in the upwelling system[mol/kg]
$T_m^i(z)$	mixed layer tracer concentration in the upwelling system [mol/kg]
$T^i(-H_{mix})$	tracer concentration at the bottom of the mixed layer [mol/kg]
N, D, O	concentrations of the Tracers Nutrients, Detritus and Oxygen [mol/kg]

abbreviation	long form	meaning
$w(z)$	see eq. (73)	vertical advection velocity in the system
$w_t(z)$	$w(z) + w_s$	vert. velocity of sinking detritus in system
ξ	$l_d \frac{H - H_{mix}}{w_e}$	

3.2 The Tracer Properties

In the following chapters the behavior of different tracers in a water column is described. A short introduction into the properties of the tracers is given now.

active/passive tracers

An active tracer influences the density of the seawater, it is dissolved in. Salinity is a good example for an active tracer. The tracers of interest in the following models (oxygen, detritus, nutrients) are described as passive tracers.

conservative/non-conservative tracers

Conservative tracers are not affected by chemical or biological processes in the water. For example salinity can well be modeled as a conservative tracer. Oxygen, detritus and nutrients are consumed/produced and transformed into other tracers. Therefore they are treated as non-conservative tracers in the model. The total amount of elementary tracers $\sum_i N_i$ is conserved in the process.

3.3 Passive, Sinking Tracer

Now a certain concentration of tracers occurring in the mixed layer is assumed - for example detritus formed by the phytoplankton and zooplankton. This tracer is heavier than the surrounding water, giving it a certain sinking velocity w_s. The sinking velocity w_s and the upwelling velocity $w(z)$ add up to the combined velocity $w_t(z)$. For the moment a constant upwelling velocity is assumed again so that w_t is constant. If this detritus is now sinking from the mixed layer, the differential equation is

$$\frac{\partial}{\partial z} w_t D(z) = 0 \tag{58}$$

Setting a starting point for the integration on the bottom of the mixed layer and integrating downwards, the solution for the detritus profile is

$$-\int_{-H_{mix}}^{z} w_t D(z) = 0 \Rightarrow D(z) = D(-H_{mix}) \tag{59}$$

Since detritus gets mineralized while sinking, it is a non conservative tracer. A loss term proportional to the detritus concentration in the water is introduced. Integrating the resulting equation in the same way as done before without the loss term, the result is an exponentially decreasing profile for the Detritus concentration.

$$\begin{aligned} \frac{\partial}{\partial z} w_t D(z) &= -l_d D(z) \\ D(z) &= D(-H_{mix}) \exp\left(-\frac{l_d}{w_t}(z + H_{mix})\right) \end{aligned} \tag{60}$$

The scale length is w_t/l_d. For example, for $w_t = 10\frac{\mathrm{m}}{\mathrm{d}}$ and $l_d = 0.01\mathrm{d}^{-1}$, the scale length would be 1000m.

3.4 Tracer Transport in a round Upwelling Area

A basic transport equation for such tracers considering advection and diffusion of the tracer and arbitrary sources and sinks is

$$\frac{\partial T}{\partial t} + \nabla_H \cdot \mathbf{u_H} T + \frac{\partial (w + w_s) T}{\partial z} - A_H \Delta_H T - A_V \frac{\partial^2 T}{\partial z^2} = \sum_i S_i. \tag{61}$$

Horizontally integrated quantities can be introduced by integrating the equations over the area of the upwelling system.

$$\langle T(z,t) \rangle = \int_0^R dr\, r \int_0^{2\pi} d\varphi T(\varphi, z, t) \tag{62}$$

In the same way integrated quantities over the lateral boundaries are introduced.

$$\bar{T}(z,t) = \int_0^{2\pi} d\varphi R T(t, \varphi, z, t) \tag{63}$$

Taking the cylindrical geometry into account by using the operators from eq. (19) and applying the integrals, we get a tracer equation for our special symmetry.

$$\begin{aligned} \int_0^R dr\, r \int_0^{2\pi} d\varphi \frac{1}{r} \frac{\partial r u_r T}{\partial r} &= \int_0^{2\pi} d\varphi\, R u_r T|_0^R = \overline{u_r T}, \\ A_H \int_0^R dr\, r \int_0^{2\pi} d\varphi \frac{1}{r} \frac{\partial}{\partial r}\left(r \frac{\partial T}{\partial r}\right) &= A_H \int_0^{2\pi} d\varphi \left(r \frac{\partial T}{\partial r}\right)\Big|_0^R = \overline{A_H \frac{\partial T}{\partial r}} \end{aligned} \tag{64}$$

With this definitions, we can now express (61) for the integrated quantities.

$$\frac{\partial \langle T \rangle}{\partial t} + \overline{u_r T} + \frac{\partial \langle (w + w_s) T \rangle}{\partial z} - \overline{A_H \frac{\partial T}{\partial r}} - A_V \frac{\partial^2 \langle T \rangle}{\partial z^2} = \sum_i \langle S_i \rangle \tag{65}$$

Except for section 3.9, a model in steady state with only advective fluxes is created, keeping the equations first order and suitable for analytic treatment.

$$\overline{u_r T} + \frac{\partial \langle (w + w_s) T \rangle}{\partial z} = \sum_i \langle S_i \rangle \tag{66}$$

For a uniformly distributed tracer of concentration $T = 1$, the volume conservation is retained.

$$\overline{u_r} + \frac{\partial \langle w \rangle}{\partial z} = 0. \tag{67}$$

The divergence in the vertical flow is balanced by horizontal fluxes. Now a rigid-lid boundary condition is introduced for the sea surface, the sea bottom is assumed to be flat. Thus we can assume, that in the area integrated equations, no vertical fluxes are existent at the surface and the sea bottom. The vertical derivative if w must change its sign somewhere in the water column and the vertical integral vanishes.

$$\int_{-H}^0 \frac{\partial \langle w \rangle}{\partial z} \mathrm{d}z = \langle w(z = 0) \rangle - \langle w(z = -H) \rangle = 0 \tag{68}$$

The vertical boundary conditions make the lateral flux through the boundary conditions of the system vanish. The tracer concentration in the upwelling area are only changed, if there is a difference in the typical tracer concentration outside of the upwelling area (T^o) and and the horizontal average tracer concentration inside the upwelling area($T^i(z)$). For the fluxes through the lateral boundaries of the upwelling system, an "upwind" specifica-

tion is appropriate for a simplified model,

$$u_r T = \theta(u_r)T^i + \theta(-u_r)T^o. \tag{69}$$

The vertical tracer flux through the mixed layer depth is also modeled using an upwind specification

$$wT = \theta(w)T_b + \theta(-w)T_m. \tag{70}$$

The hydrodynamical model showed that circular shaped, rotational wind stress leads to a cylindrical upwelling geometry (see e.g. section 2.7.3). The vertical velocity has its maximum at $z = -H_{mix}$ and decreases to the surface and the bottom.
We assume that the wind induces a uniform vertical upwelling velocity at the bottom of the mixed layer. Recalling the model results from section 2, we are approximating the vertical velocity within the wind influenced upwelling area with the formula

$$w(z) = w_e \left(\theta(H_{mix} + z)\frac{-z}{H_{mix}} + \theta(-H_{mix} - z)\frac{z + H}{H - H_{mix}} \right). \tag{71}$$

Further we assume that the mixed layer depth is equivalent to the depth of the eophotic zone. In section (2.7.3) it can be seen, that the upwelling is sharply limited to the extend of the wind field. If a forcing only has a rotational component, the resulting currents have a polar symmetric structure. The continuity equation (3) can be written in polar coordinates.

$$\frac{1}{\rho}\frac{\partial}{\partial \rho}(\rho u_\rho) + \frac{\partial w}{\partial z} = 0. \tag{72}$$

Solving this equation for the radial velocity at the outer boundary of the system, a velocity is derived, which will be denoted as u_r.

$$u_r(z) = \frac{R w_e}{2} \left(\theta(z + H_{mix})\frac{1}{H_{mix}} - \theta(-z - H_{mix})\frac{1}{H - H_{mix}}) \right) \tag{73}$$

Under the mixed layer a constant current u_r is entering the system, in the mixed layer it is leaving with a constant velocity. The tracer concentrations inside an upwelling area are influenced by the tracer concentration in the lower layer T_b^o, the tracer concentrations inside a downwelling area are influenced by the tracer conctration in the mixed layer T_m^o. With given concentration of the tracers outside of the system (boundary conditions) e.g. from measurements, the tracer import into the system can be determined. In this work, we assume constant tracer concentrations outside of the upwelling area.

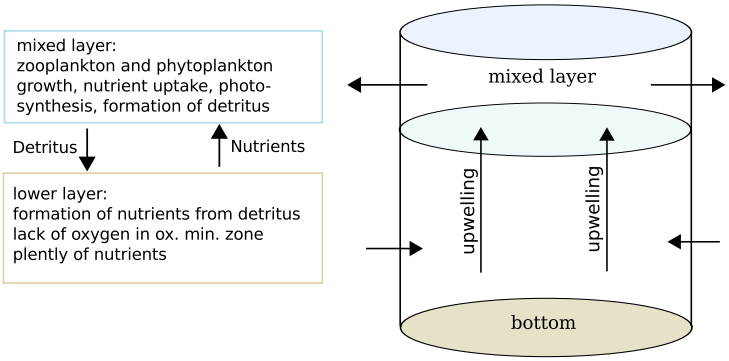

Figure 6: *Nutrient and oxygen rich deep-water is entering the upwelling area below the mixed layer and is advected upwards. It is leading to an increased bioactivity, detritus is produced in the mixed layer. The detritus is sinking and is mineralized during its way down, depleting oxygen in the process.*

3.4.1 Mineralization and Photosynthesis

To describe the dynamics of oxygen, nutrients and detritus in the system, different equations for the mixed layer and the lower layer are used. In general, the equations are first order differential equations with an advection/sinking term and a production/loss term. An example making a first approach on including diffusion into the equations is given in section 3.9.The concentration of oxygen and nutrients outside of the system is assumed to be homogeneous in the bottom layer. For the moment, oxic conditions are assumed for the whole water body, so that the process of mineralisation uses up this dissolved oxygen according to

$$(CH_2O)_{106}(NH3)_{16}H_3PO_4 + 106O_2 \rightarrow 106CO_2 + 16NH_3 + H_3PO_4 + 106H_2O \quad (74)$$

thus the oxygen demand to recycle nitrogen in the model is set to be $s_2 = \frac{106}{16} = 6.625$ (e.g. Fennel and Neumann 2004,Martin Schmidt and Eggert 2012). If the molecular oxygen in the water is used up, other chemical processes are taking over. The oxygen needed to mineralize detritus is taken from nitrate under anoxic conditions.

$$(CH_2O)_{106}(NH_3)_{16}H_3PO_4 + 84.4HNO_3 \rightarrow 106CO_2 + 16NH_3 + 42.4N_2 + H_3PO_4 + 148.8H_2O \quad (75)$$

or, if nitrate is exhausted, sulphate is reduced according to

$$(CH_2O)_{106}(NH_3)_{16}H_3PO_4 + 53H_2SO_4 \rightarrow 106CO_2 + 53H_2S + H_3PO_4 + 106H_2O + 16NH_3. \quad (76)$$

In general, the oxygen consumption is described according to (74) with the stochiometrix ratio s_2. Mainly systems with oxic conditions are considered, but we keep in mind that a

negative oxygen concentration would correspond to the reactions (75) or (76).

The limiting nutrient in the system is assumed to be nitrogen. It is tracked just by counting present nitrogen atoms, not differentiating further between nitrate or ammonium. Only the difference between nitrogen in detritus and biologically available nitrogen is made. In the mixed layer the inverse process, the photosynthesis is happening:

$$106CO_2 + 16NH_3 + H_3PO_4 + 106H_2O \rightarrow (CH_2O)_{106}(NH3)_{16}H_3PO_4 + 106O_2 \quad (77)$$

3.4.2 The Model Equations

To model the depth dependent tracer equations in the model for oxygen, detritus and nutrients, equation (66) is used. The mineralization process is a sink in the detritus and the oxygen concentration and a source in the nutrients equation. Boundary values for the concentrations of oxygen and nutrients (O_b^o, N_b^o) in the lower layer are introduced. The concentration of detritus in the deep water outside of the upwelling geometry is assumed to be zero, thus the lateral advection term in the detritus equation vanishes. The upstream scheme is used to describe the advective transport of water masses with this outside concentrations into the model geometry.

$$\begin{aligned} \pi R^2 \frac{\partial}{\partial z}\left(w_t(z) D_b^i(z)\right) &= -\pi R^2 l_d D_b^i(z) \\ 2\pi R u_r^u O_b^o + \pi R^2 \frac{\partial}{\partial z}\left(w(z) O_b^i(z)\right) &= -\pi R^2 l_d s_2 D_b^i(z) \\ 2\pi R u_r^u N_b^o + \pi R^2 \frac{\partial}{\partial z}\left(w(z) N_b^i(z)\right) &= \pi R^2 l_d D_b^i(z). \end{aligned} \quad (78)$$

To treat these equations numerically, they can be rewritten in the form

$$\begin{aligned} \frac{\partial D_b^i}{\partial z} &= \frac{1}{w_t(z)}\left(-l_d D_b^i(z) - \frac{\partial w(z)}{\partial z} D_b^i(z)\right) \\ \frac{\partial O_b^i}{\partial z} &= \frac{1}{w(z)}\left(\frac{\partial w(z)}{\partial z}\left(O_b^o - O_b^i(z)\right) - l_d s_2 D_b^i(z)\right) \\ \frac{\partial N_b^i}{\partial z} &= \frac{1}{w(z)}\left(\frac{\partial w(z)}{\partial z}\left(N_b^o - N_b^i(z)\right) + l_d D_b^i(z)\right). \end{aligned} \quad (79)$$

3.5 Derivation of the Detritus Profile

No we will take a closer look at the sinking detritus, we started with in chapter 3.3. In equation (60), the vertical velocity canceled out, it was assumed to be constant at

that point. A discussion of a tracer with accelerating sinking speed is done in Kriest and Oschlies 2008. Here a new approach is made, the vertical velocity of the detritus is assumed to be a superposition of its falling speed w_s (negative value) and the upwelling velocity $w(z)$ according to (71).

$$w_t(z) = w(z) + w_s \tag{80}$$

Because $w_t(z)$ is dependent of the vertical coordinate z, it does not cancel out anymore. The new equation for $D_b^i(z)$ is:

$$\begin{aligned} w_t(z)D_b^i(z) &= w_t(-H_{mix})D_b^i(-H_{mix})\exp\left(-q(z,H_{mix})\right) \\ & \qquad \text{with} \\ q(z,H_{mix}) &= \int_{-H_{mix}}^{z} \frac{l_d}{w_t(z)}\mathrm{d}z \end{aligned} \tag{81}$$

Solving the integral (81) with the definition for $w_t(z)$ according to (80) and (71) we get:

$$q(z,H_{mix}) = l_d \frac{H - H_{mix}}{w_e} \ln\left(\frac{\frac{z+H}{H-H_{mix}} + \frac{w_s}{w_e}}{1 + \frac{w_s}{w_e}}\right) \tag{82}$$

The result for the detritus equation can be simplified further

$$\begin{aligned} w_t(z)D_b^i(z) &= w_t(-H_{mix})D_b^i(-H_{mix})\left(\frac{1 + \frac{w_s}{w_e}}{\frac{z+H}{H-H_{mix}} + \frac{w_s}{w_e}}\right)^{\left(l_d\frac{H-H_{mix}}{w_e}\right)} \\ D_b^i(z) &= D_b^i(-H_{mix})\left(\frac{w_e + w_s}{w_t(z)}\right)^{\left(l_d\frac{H-H_{mix}}{w_e}+1\right)} \end{aligned} \tag{83}$$

The term $\frac{l_d}{w_e}(H - H_{mix})$ appears often in the derivations in this section, therefore the abbreviation

$$\frac{l_d}{w_e}(H - H_{mix}) = \xi \tag{84}$$

is introduced.

Forming the limit $w_e \to 0$:

$$D_b^i(z) = D(-H_{mix})\exp\left(-\frac{l_d}{w_s}(z + H_{mix})\right) \tag{85}$$

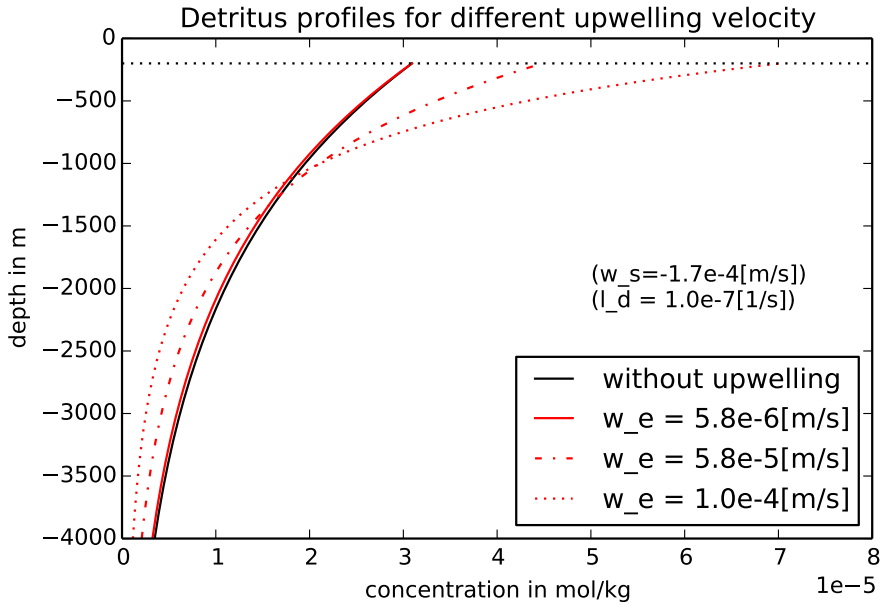

Figure 7: *Effect of the upwelling velocity on the detritus profile. A constant detritus flux from the mixed layer into the lower layer is used as a boundary condition here. Without upwelling, equation (83) equals (60). With increasing upwelling velocity, the detritus is longer suspended in the water so the amount of detritus reaching the sea floor is lower.*

Without vertical velocity variation, the result for the detritus profile equals (60) again.

Evaluating (83) at the bottom $z = -H$, the detritus concentration is

$$D_b^i(-H) = D_b^i(-H_{mix}) \left(\frac{w_e + w_s}{w_s} \right)^{\xi+1} . \tag{86}$$

If the upwelling velocity is close to the sinking velocity ($w_e \to w_s$), (86) becomes zero. The detritus is suspended a long time under the bottom of the mixed layer in that case, leading to an almost complete mineralization before it reaches the ground.

3.6 Advection-Consumption Equation for Oxygen

Having derived the detritus profile, it is now possible to solve the differential equation for the oxygen profile from equation set (78).

$$2\pi R u_r O_b^O + \pi R^2 \frac{\partial}{\partial z} \left(w(z) O_b^i(z) \right) = -\pi R^2 s_2 l_d D_b^i \tag{87}$$

The oxygen concentration outside of the system is assumed to have a constant concentra-

tion O_b^o throughout the whole lower water layer. As a passive tracer the oxygen is then advected into the system and depleted by the mineralisation process. In the mixed layer, oxygen is released again due to photosynthesis.
By inserting the term for u_r from the lateral advection equation (73) and the detritus profile (83), the equation can be written as

$$\frac{\partial}{\partial z}\left(w(z)O_b^i(z)\right) = -l_d s_2 D_b^i(z) + \frac{w_e}{H - H_{mix}} O_b^o \tag{88}$$

The detritus profile derived in the previous subsection is inserted for $D_b^i(z)$ with the boundary condition of a constant flux at $z = -H_{mix}$. Integration from $-H$ to z delivers:

$$\begin{aligned} & w(z)O_b^i(z) - w(-H)O_b^i(-H) \\ =& s_2 D_{mix}(w_e + w_s)\left[\left(\frac{w_e + w_s}{w_t(z)}\right)^{\xi} - \left(\frac{w_e + w_s}{w_s}\right)^{\xi}\right] + w_e \frac{z + H}{H - H_{mix}} O_b^o \end{aligned} \tag{89}$$

The vertical velocity at the sea ground is 0 as defined in (71). With the definitions in (71) and (80), the result can be rewritten to

$$O_b^i(z) = O_b^o + s_2 D_{mix}\left(\frac{w_e + w_s}{w(z)}\right)\left[\left(\frac{w_e + w_s}{w_t(z)}\right)^{\xi} - \left(\frac{w_e + w_s}{w_s}\right)^{\xi}\right] \tag{90}$$

The oxygen is entering the system in the lower layer and is depleted by the mineralisation process. Depending on the amount of available nutrients (N), a negative oxygen concentration can occur in this very simple model.

3.7 Advection-Consumption Equation for Nitrogen

The profile for the nutrients can be derived analogously. Mathematically, the equation

$$2\pi R u_r^u N_b^o + \pi R^2 \frac{\partial}{\partial z}\left(w(z)N_b^i(z)\right) = \pi R^2 l_d D_b^i(z) \tag{91}$$

is quite similar to the equation for the oxygen (90), leading to the solution

$$N_b^i(z) = N_b^o - D_b^i(-H_{mix})\frac{(w_e + w_s)}{w(z)}\left[\left(\frac{w_e + w_s}{w_t(z)}\right)^{\xi} - \left(\frac{w_e + w_s}{w_s}\right)^{\xi}\right]. \tag{92}$$

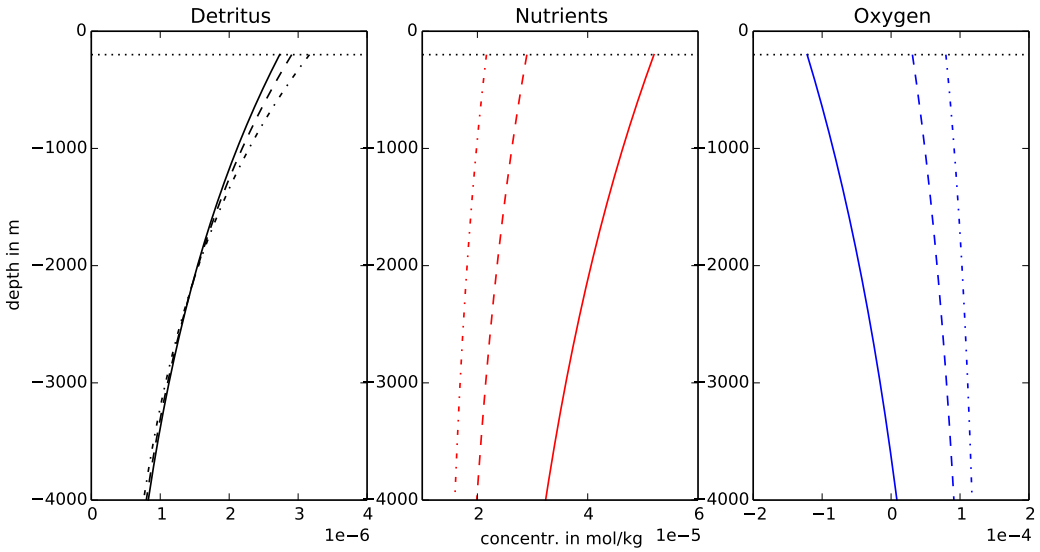

Figure 8: *Tracer profiles with given constant flux boundary condition of detritus import from the surface layer (see subsection 3.3).*
Parameters: $w_s = -5.74 \cdot 10^{-4} m/s$ $w_e = 2.5 \cdot 10^{-5} m/s$ *(solid line);* $w_e = 5.8 \cdot 10^{-5} m/s$ *(dashed line);* $w_e = 1.0 \cdot 10^{-4} m/s$ *(dash-dotted line);* $N_b^o = 1.1 \cdot 10^{-5} mol/kg$ *;* $O_b^o = 1.5 \cdot 10^{-4} mol/kg$*; detritusflux from mixed layer:* $(w_e + w_s)D_{mix} = 1.5 \cdot 10^{-9} (m\ mol)/(s\ kg)$*;* $H = 4000m$*;* $H_{mix} = 200m$*;* $l_d = 1.7 \cdot 10^{-7} s^{-1}$.
The solution for the detritus differential equation (83) has an antiexponential character. A nutrient assimilation in the system can be seen, the concentration for the nutrient is ,in the water column within the upwelling area, significantly higher than the given outside nutrient concentration. The mineralization process of the detritus is using up oxygen, a minimum of the oxygen can be seen directly under the bottom of the mixed layer.

The concentration profiles for oxygen and nutrient are consistent of the basic tracer concentration outside of the system T_b^o and a term that arises from the mineralization process, which is depleting oxygen and producing nutrients.

Nutrients are entering the system at the lateral boundaries and are leaving it by advection in the mixed layer or they are assimilated into biomass.

3.8 Nutrient Accumulation in an Upwelling Area without lateral Export of Nutrients

In section 3.6 and 3.6, a system with a fixed boundary condition for the detritus flux from the mixed layer was considered. There has been no feedback of the processes happening in the mixed layer on the water below. Now a new boundary condition at $z = -H_{mix}$ is used. All nutrients that are transported into the mixed layer are transformed to detritus and immediately returned into the lower layer. The system is closed and no nutrients are leaving the system by advection in the mixed layer any more. The new flux boundary condition is

$$w_e N_b^i(-H_{mix}) = -(w_e + w_s) D^i(-H_{mix}). \tag{93}$$

The general solution for the depth dependent nutrient profile for a given detritus flux into the system has already been derived (92). Evaluating (92) at the depth $z = -H_{mix}$

$$w_e N_b^i(-H_{mix}) = w_e N_b^o - w_e D_b^i(-H_{mix}) \frac{w_e + w_s}{w_e} \left(1 - \left(\frac{w_e + w_s}{w_s}\right)^{\xi}\right) \tag{94}$$

and inserting the boundary condition (93) for $D(-H_{mix})$, we get an equation determining the flux of nutrients through the surface layer

$$w_e N_b^i(-H_{mix}) = w_e N_b^o \left(\frac{w_s}{w_e + w_s}\right)^{\xi}. \tag{95}$$

By setting this boundary condition, we don't have to express the nutrient equation in dependence of the incoming detritus anymore. Instead the detritus flux is expressed by nutrient export into the mixed layer. The incoming nutrients themselves are only dependent of the concentration outside of the geometry (and the advective velocities of course). It is visible now, that there is a nutrient accumulation, increasing the concentration of nutrients at $z = -H_{mix}$ by the factor $\left(\frac{w_s}{w_e+w_s}\right)^{\xi}$ compared to the background concentration in the surrounding water. The factor is dependent on the vertical velocities, the

dept of the lower layer ($H - H_{mix}$) and the conversion rate l_d. For small l_d, the nutrient enrichment disappears due to the inefficiency of the mineralisation process. In a closed system, equation (92) with the new boundary conditions becomes

$$N_b^i(z) = N_b^o + \frac{w_e}{w(z)} N_b^o \left(\left(\frac{w_s}{w_t(z)} \right)^{\xi} - 1 \right). \tag{96}$$

The concentration of nutrients consists of the concentration N_b^o plus an enrichment term.

Now we can use our flux boundary also for the equation derived in the (82) and get for the detritus profile in a closed system

$$D_b^i(z) = -\frac{w_e}{w_t(z)} N_b^o \left(\frac{w_s}{w_t(z)} \right)^{\xi} \tag{97}$$

and finally also for the oxygen profile

$$O_b^i(z) = O_b^o - s_2 \frac{w_e}{w(z)} N_b^o \left(\left(\frac{w_s}{w_t(z)} \right)^{\xi} - 1 \right). \tag{98}$$

Evaluating the equation for the detritus flux at the bottom of the ocean

$$\pi R^2 w_t(-H) D_b^i(-H) = -\pi R^2 w_e N_b^o = 2\pi R u_r^o N_b^o, \tag{99}$$

the flux equals the one for the nutrients entering the system through the lateral boundaries. The only nitrogen sink in this system is the sedimentation of detritus.

It is not trivial to see the behavior of (98) or (96) for $w_e \to 0$ or at the bottom at $z = -H$. The application of l'Hospital's rule (e.g. Furlan 2010) is useful.

Taking the limiting value for $z \to -H$ of the tracer profiles (with the help of l'Hospital's rule), the bottom concentrations are derived

$$\begin{aligned} N_b^i(-H) &= N_b^o - \frac{l_d}{w_s}(H - H_{mix}) N_b^o \\ O_b^i(-H) &= O_b^o + s_2 \frac{l_d}{w_s}(H - H_{mix}) N_b^o \\ D_b^i(-H) &= -\frac{w_e}{w_s} N_b^o. \end{aligned} \tag{100}$$

The detritus concentration at the bottom is independent of the conversion rate l_d and the depth of the water. It only depends on the sinking velocity of the detritus, the maximum

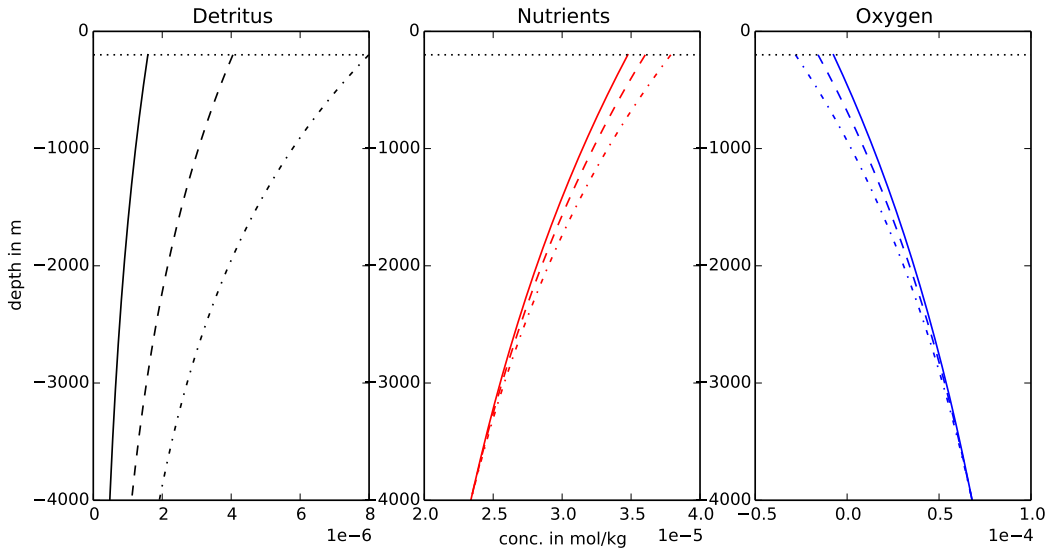

Figure 9: *Tracer profiles of ecosystem model without advective export in the mixed layer, derived in subsection 3.8. All nutrients exported into the mixed layer are returned as detritus. Parameters:* $w_s = -5.74 \cdot 10^{-4} m/s$; $w_e = 2.5 \cdot 10^{-5} m/s$ *(solid line);* $w_e = 5.8 \cdot 10^{-5} m/s$ *(dashed line);* $w_e = 1.0 \cdot 10^{-4} m/s$ *(dash-dotted line);* $N_b^o = 1.1 \cdot 10^{-5} mol/kg$; $O_b^o = 1.5 \cdot 10^{-4} mol/kg$; $H = 4000m$; $H_{mix} = 200m$; $l_d = 1.7 \cdot 10^{-7} s^{-1}$.
In this case all the nutrient that is entering the system through the lateral boundaries is getting lost by sedimentation of the detritus at the bottom of the sea. A stronger nutrient enrichment and oxygen minimum zone and more detritus are forming, compared to fig. 8.

upwelling velocity and the concentration of nutrients outside of the system. This must be due to the model geometry and the boundary condition, equations (85) and (83) are still showing a dependency of l_d at the sea bottom.

In contrast to the detritus concentration, the bottom concentrations of N_b^i and O_b^i are dependent of the conversion rate l_d, the thickness (depth) of the lower water layer $(H - H_{mix})$ and the sinking velocity.
It is noteworthy, that the bottom concentrations of N_b^i and O_b^i do not depend on the maximum upwelling velocity w_e. Recall, that the divergence of the vertical velocity is balanced by the horizontal advection, thus the nutrient import is proportional to w_e. Due to the boundary condition (93) the production of detritus is also proportional to w_e.
For small w_e, the vanishing detritus production could lead to the assumption, that the nutrient enrichment and the oxygen minimum must vanish. However, the duration the water is staying in the system also becomes very large.
It seems funny, that the equations for the concentrations in steady state are not con-

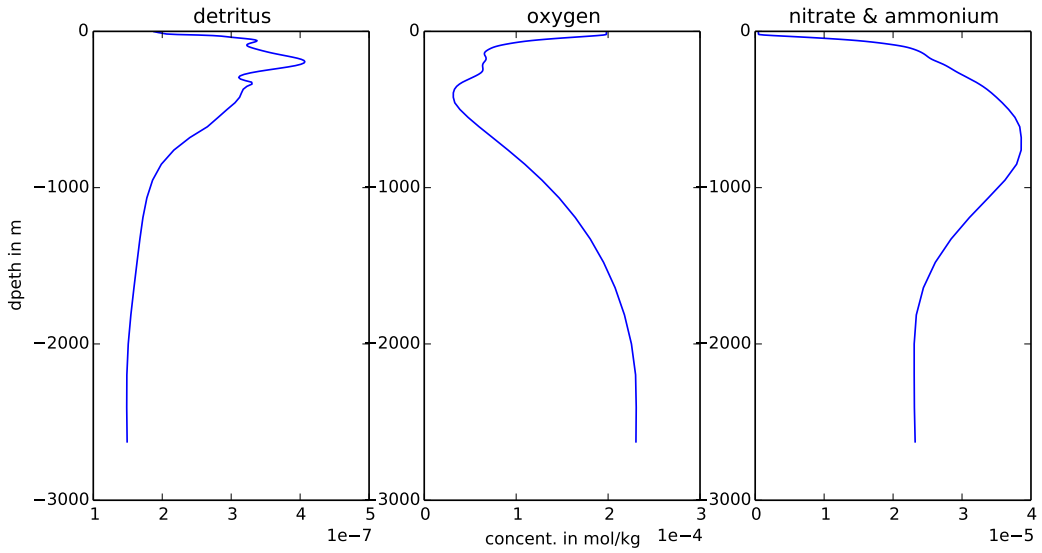

Figure 10: *Profiles from a more complex numerical model (Modular Ocean Model, model run 81, at Institut für Ostseeforschung Warnemünde). The concentrations of detritus, oxygen and nitrate+ammonium are shown at approximately* $10°S$, $10°E$, *the location of the "Angola Dome" upwelling area. In greater depth under the mixed layer, the same features for the tracer profiles can be seen as for the analytical model.*

tinuous, when varying w_e. For $w_e = 0$, no detritus is produced in the model and the concentrations in the model geometry should be equal to the background concentrations. The equations (100) show a constant difference from the background concentration, which does not vanish for $w_e \to 0$. This interesting behavior should be subject to further investigations, but it is beyond the scope of this work.

3.9 The Effect of Diffusion

To study the effect of diffusion close to the mixed layer, a diffusion term is added to the oxygen equation in (78) and the vertical velocity is approximated as constant (see fig. 11) . This approximation can only be applied to a small depth range, otherwise it would violate the boundary conditions (68). The diffusion A_v is approximated as constant in $\triangle z$. For a constant upwelling velocity, the divergence and, in consequence, the lateral advection term are vanishing

$$w\frac{\partial O}{\partial z} - A_v\frac{\partial^2 O}{\partial z^2} = -l_d D(z). \tag{101}$$

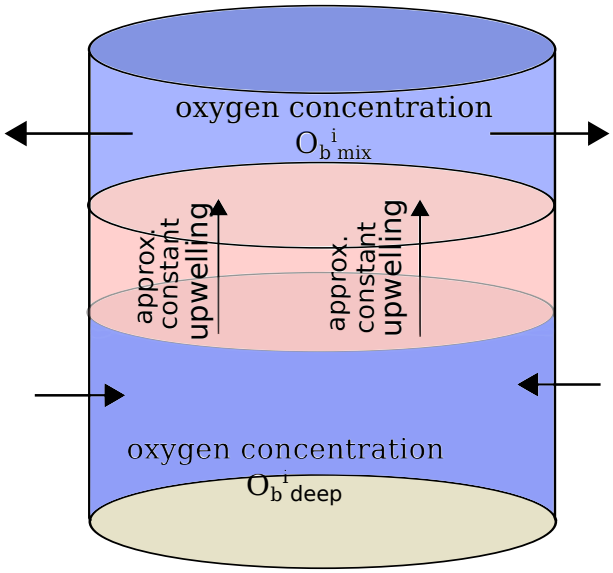

Figure 11: *Close to the mixed layer, the tracer equations may be influenced by vertical mixing. As discussed in section 3.8, the oxygen minimum and the nutrient maximum can be found in greater depth in more realistic models. The model equations (78) are therefore extended with a diffusion term. The vertical velocity in a limited depth range $\triangle z$ close to the mixed layer, is approximated as constant.*

The addition of a diffusion term to the tracer equation increases the order of the differential equation to second order. Thus, two boundary conditions are required. For the water, that is getting upwelled from the depth, a typical concentration for oxygen in the deep ocean

$$O_b^i(-H_1) = O_{b,deep}^i \tag{102}$$

is used. In the mixed layer, a constant oxygen concentration is maintained by the contact with the atmosphere and turbulent mixing

$$O_b^i(-H_{mix}) = O_{b,mix}^i. \tag{103}$$

The water from the mixed layer is not entering the system by advection, but it affects the oxygen concentration through the diffusion term and is forming the second boundary condition to the differential equation 101. Some approaches how to deal with advection-diffusion equations are presented in David M. Glover, Jenkins, and Doney 2011. With the profile from equation (85), it is possible to solve the differential equation for a constant upwelling velocity.

This time we are considering an advection diffusion equation like in (65) but with constant

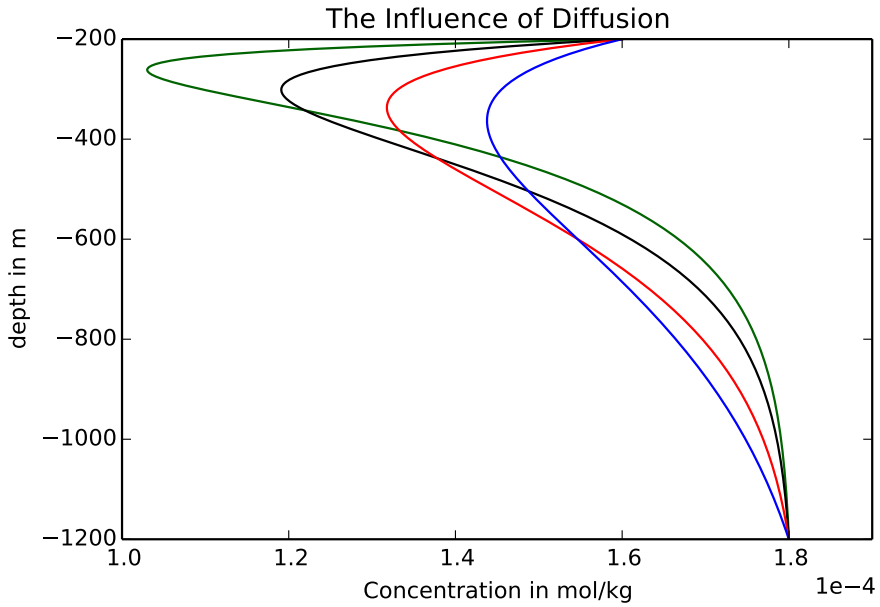

Figure 12: *This plot shows the solution (111) of the differential equation for oxygen with an additional diffusion term and constant vertical velocity. The different profiles are for the different diffusion constants* $A_v = 2 \cdot 10^{-4} \frac{m^2}{s}$ *(green),* $A_v = 5 \cdot 10^{-4} \frac{m^2}{s}$ *(black),* $A_v = 10^{-3} \frac{m^2}{s}$ *(red),* $A_v = 2 \cdot 10^{-3} \frac{m^2}{s}$ *(blue). The other parameters for this plot are:* $O^i_{b,mix} = 1.6 \cdot 10^{-4} \frac{mol}{kg}$, $O^i_{b,deep} = 1.8 \cdot 10^{-4} \frac{mol}{kg}$, $D_{mix} = 3.8 \cdot 10^{-6} \frac{mol}{kg}$, $w_e = 5.8 \cdot 10^{-7} \frac{m}{s}$, $w_t = -1.74 \cdot 10^{-4} \frac{m}{s}$, $l_d = 10^{-6} \frac{1}{s}$, $H = 1200m$, $H_{mix} = 200m$. *The approximation for a constant upwelling velocity can only done in a smaller depth range, so it is not violating the bottom and surface boundary conditions.*

vertical velocity

$$\pi R^2 w_e \frac{\partial}{\partial z} O_b^i(z) - \pi R^2 A_v \frac{\partial^2 O_b^i(z)}{\partial z^2} = \pi R^2 l_d D_b^i(z) \tag{104}$$

The homogeneous differential equation can be reduced in order:

$$\frac{\partial X(z)}{\partial z} - \frac{w_e}{A_v} X = 0 \tag{105}$$

The solution of the homogeneous reduced differential equation is:

$$X(z) = c_1 \exp\left(\frac{w_e}{A_v} z\right) \tag{106}$$

A particular solution can be found by variation of the integration parameter:

$$\frac{\partial X(z)}{\partial z} = \frac{\partial c_1(z)}{\partial z} \exp\left(\frac{w_e}{A_v} z\right) + c_1(z) \frac{w_e}{A_v} \exp\left(\frac{w_e}{A_v} z\right) \tag{107}$$

Substituting this into the reduced, inhomogeneous differential equation

$$\begin{aligned} \frac{\partial c_1(z)}{\partial z} &= \frac{l_d D_b^i(z)}{A_v} \exp\left(-\frac{w_e}{A_v} z\right) \\ &\approx \frac{l_d}{A_v} D_b^i(-H_{mix}) \exp\left(-\frac{l_d}{w_e + w_s}(z + H_{mix}) - \frac{w_e}{A_v} z\right) \end{aligned} \tag{108}$$

Finally we get the $c_1(z)$ for the particular solution of the the reduced inhomogeneous differential equation.

$$X = X_h + X_p = c_1 \exp\left(\frac{w}{A_v} z\right) - \frac{l_d D_b^i(-H_{mix})}{A_v \left(\frac{l_d}{w_e + w_s} + \frac{w_e}{A_v}\right)} \exp\left(-\frac{l_d}{w_e + w_s}(z + H_{mix})\right) \tag{109}$$

Integrating over the depth gives the solution of the original (non reduced) differential equation

$$O_b^i(z) = \frac{A_v}{w_e} c_2 \exp(\left(\frac{w_e}{A_v} z\right) - \underbrace{\frac{D_b^i(-H_{mix})}{\frac{A_v}{w_e + w_s}\left(\frac{l_d}{w_e + w_s} + \frac{w_e}{A_v}\right)}}_{\text{b}} \exp\left(-\frac{l_d}{w_e + w_s}(z + H_{mix})\right) + c_3. \tag{110}$$

By setting the boundary conditions (102) and (103) for the bottom of the mixed layer and the depth $-H_1$ (which must not be the bottom in this case because of the assumed

constant w), it follows

$$O_b^i(z) = O_{b,mix}^i + \left[O_{b,deep}^i - O_{b,mix}^i + \frac{D(-H_{mix})}{b} \left(1 - \exp\left(-\frac{l_d}{w_t}(H_{mix} - H) \right) \right) \right] \cdot \frac{1 - \exp\left(\frac{w_e}{A_v}(z + H_{mix}) \right)}{1 - \exp\left(\frac{w_e}{A_v}(-H + H_{mix}) \right)} - \frac{D(-H_{mix})}{b} \left(1 - \exp\left(-\frac{l_d}{w_t}(z + H_{mix}) \right) \right). \quad (111)$$

The profile of the oxygen concentration (see fig. 10) shows a minimum somewhat below the mixed layer. A comparison with profiles from a more complex numerical model (see fig. 10) shows that this process of downmixing of oxygen from the mixed layer is indeed present. Stronger upwelling velocity is moving the oxygen minimum upwards. More diffusion is bringing the oxygen minimum zone downwards. Less diffusion in combination with a low upwelling velocity (and a high detritus concentration) is followed by a distinct oxygen minimum.

4 Results and Summary

Beginning with the linearized Boussinesq equations, wind driven ocean currents were derived. The volume forcing of the winds is confined to the mixed layer, and in consequence the upwelling velocity's maximum w_e is close to the bottom of the mixed layer.
The water circulation found follows two different patterns. In the first (circular) wind field with homogeneous wind (38), the rotation of the wind field at the two wind edges has a different sign, causing upwelling on one side and downwelling on the other. Integrated over the whole area, the upwelling vanishes, just like the wind rotation does.
The fact that the area integrated upwelling vanishes is also the reason, that there are no counter currents outside of the wind field in contrast to the other wind-driven current fields. A transport of water from the upwelling area to the downwelling area is establishing and a counter directed current in the depth is transporting the water back to its origin (see fig 3).
The other two analyzed wind fields (44) and (53) are polar symmetric. Polar symmetric wind fields also cause polar symmetric current-fields in the f-plane approximation. For cyclonic wind forcings, the water is entering the wind influenced area below the bottom of the mixed layer and leaving it to the sides in the mixed layer. For the analyzed rotational winds, the maximum of the upwelling is happening in the middle of the upwelling area, decreasing to the lateral boundaries (see figures 4 and 5).
The currents caused by a purely rotational, cyclonic wind forcing were used as a scheme

to describe the advection of tracers in a simple ecosystem model.
For the rotational (polar symmetric) wind structures, the pressure perturbation has the same sign within the whole wind influenced area, causing large scaled up/downwelling. The pressure perturbations caused by the wind fields always include one term that is growing linearly in time. The linearly growing term in the pressure equation causes a constant upwelling. In our simple model, the pressure perturbation can grow indefinitely large and is in geostrophic balance with an also linearly growing angular velocity. There is no process stopping the pycnocline from getting constantly more elevated. To make the model more realistic, turbulent downmixing of the pycnocline could be included into the equations.
For the influence of the wind driven tracer transport processes on the ecosystem, the angular rotation velocity of the mass in a polar symmetric system is irrelevant. There are no angular tracer gradients.
Assuming a cyclonic wind forcing like in subsection 2.7.3 and 2.7.4 is acting on the open ocean, water masses are transported into the upwelling area in the lower layer. With the currents follow tracer concentrations typical to the deep open ocean. This concentrations, taken from measurements or more advanced numerical models, are forming the boundary conditions of the model system. The upwelling of free nitrate and oxygen from the deep water causes an increased ecosystem activity.
To describe the profile of the detritus flux, the empirical "Martin Profile" (Martin et al. 1987) is often used. Another approach is a given detritus import with a constant mineralization rate and constant sinking speed (see e.g. Kriest and Oschlies 2008 or Capone et al. 2008). The approach used in this work is a linear velocity profile. It depends on D_{mix},w_s,w_e and l_d. For a vanishing upwelling velocity $w_e \to 0$, the detritus profile derived in (83) changes its shape into the form mentioned in (85), with a decay length scale of w_s/l_d.
The depth profiles for the tracers show an oxygen minimum and a nitrate maximum at the bottom of the mixed layer. The displacement for the oxygen minimum (typically it lies some hundred meters under the mixed layer) can be explained by the lack of turbulent mixing in the model. In a simpler model with constant upwelling in subsection 3.9, it was shown that the inclusion of a diffusion term parameterizing turbulent mixing can shift the depth of the oxygen minimum into a realistic depth.
Already with a fairly simple model, only considering the tracers oxygen, nutrients, detritus and a mineralization process of the detritus, it is possible to model the nutrient accumulation and the oxygen minimum zone commonly seen within an upwelling area (see fig. 8). The first approach in this work has been, to set a flux boundary condition for the amount of incoming detritus. In that case, there is no feedback of the processes

happening in the mixed layer on the lower layer. The mineralization process is assumed to be proportional to the abundance of detritus. The initial boundary concentrations of oxygen and nutrients do not have an influence on the detritus concentration and the mineralization process in the model equations.
The next step was to close the system with another flux boundary (93) between the mixed layer and the lower layer. The assumption, that all the nutrients that are leaving the system through the bottom of the mixed layer are returned as detritus, removes a sink of nutrients from the mixed layer.In the equations before, it was assumed that the nutrient export into the surface layer, that exceeds the detritus import, is lost by advection out of the geometry. The new assumption describes a system, where all nutrients entering the mixed layer are immediately processed into detritus. The missing advection sink in the mixed layer is leading to a stronger nutrient accumulation in the wind influenced upwelling area. In fact, this accumulation is happening in the whole water column, and not only close to the mixed layer (see fig. 9).
For the model with the flux boundary (all nutrients return in the form of detritus), the limiting values for the sea bottom $z = -H$ were derived in equation set (100). The third relation of (100) shows, that all the imported nutrients are sedimented as detritus. For a system without advective loss terms in the mixed layer, sedimentation becomes the only possible loss term. The equality of the lateral import of nutrients and the export into the sediment balances the equations in steady state.
It is remarkable, that the upwelling velocity does not have any influence at the nutrient and oxygen concentrations (100) at the sea bottom. The bottom concentrations are instead only determined by the conversion constant l_d, the sinking velocity w_s and the thickness of the lower water body $(H - H_{mix})$. Without upwelling, the tracer concentrations for oxygen (98) and nutrients (96) inside of the geometry are expected to be the background concentrations. In equation set (100) however, these concentrations have a constant difference from the background concentration, which does not vanish for $w_e \to 0$. To find out whether this discontinuous behavior for varying w_e is persistent in different derivations, and how it can affects other models, further investigation is needed.
In an upwelling area, the strong oxygen minimum is not only due to the nutrient enrichment and ecosystem activity, but also due to the longer suspension of the detritus in the water. If the vertical velocity is in the same order of magnitude as the sinking velocity, this gives substantially more time for detritus mineralization. Less detritus is reaching the ground and more oxygen is used up in the mineralization process.
Comparing the shape of the profiles with the ones from model runs of a more complex numerical model (fig. 10, Modular Ocean Model, model run 81, IOW), the same basic features in the shape of the profiles can be seen. The differences close to the mixed layer

were discussed in section 3.9. The similarity of the profiles is a validation, that some of the most important processes in the deep water were covered by the analytical model.

References

[AS72] M Abramowitz and I. Stegun. *Handbook of Mathematical Functions with Formulas, Graphs, and Mathematical Tables*. Dover Publications, 1972.

[Bro+08] I. Bronstein et al. *Taschenbuch der Mathematik*. Wissenschaftlicher Verlag Harri Deutsch GmbH, 2008, p. 723.

[Cap+08] Douglas G. Capone et al. *Nitrogen in the Marine Environment*. Elsevier Inc., 2008, p. 1468.

[DJD11] von David M. Glover, William J. Jenkins, and Scott C. Doney. *Modeling Methods for Marine Science*. Cambridge University Press, 2011, pp. 279, 282.

[FL89] Wolfgang Fennel and Hans Ulrich Lass. *Analytical Theory of Forced Oceanic Waves*. Akademie-Verlag Berlin, 1989.

[FN04] Wolfgang Fennel and Thomas Neumann. *Introduction to the Modelling of marine Ecosystems*. Elsevier B.V., 2004.

[Fur10] Peter Furlan. *Das gelbe Rechenbuch*. Verlag Martina Furlan, 2010, p. 181.

[KJ11] David Kadko and William Johns. "Inferring upwelling rates in the equatorial Atlantic using 7Be measurements in the upper ocean". In: *Deep-Sea Research I* 58 (2011).

[KO08] I. Kriest and A. Oschlies. "On the treatment of particulate organic matter sinking in large-scale models of marine biogeochemical cycles". In: *Biogeosciences* (2008).

[Mar+87] J. Martin et al. "carbon cycling in the Northeast Pacific". In: *Deep Sea Res.* 34 (1987).

[OBr75] J.J. O'Brien. "Numerical Models of Ocean Circulation". In: *Models of Coastal Upwelling* (1975), p. 204.

[OWE12] Dirk Olbers, Jürgen Willebrand, and Carsten Eden. *Ocean Dynamics*. Springer-Verlag Berlin Heidelberg, 2012, p. 449.

[Sch+00] M. Schmidt et al. "Data report of R/V "Poseidon" cruise 250 ANDEX'1999". In: *Meereswissenschaftliche Berichte (Marine Science Reports)* 40 (2000).

[SE12] Martin Schmidt and Anja Eggert. "A regional 3D coupled ecosystem model of the Benguela upwelling system". In: *Meereswissenschaftliche Berichte (Marine Science Reports)* 87 (2012).

[VT01] Pedro Vélez-Belchí and Joaquín Tintorí. “Vertical velocities at an ocean front”. In: *Scientia Marina* 65 (2001).

5 Danksagung

Diese Masterarbeit entstand am Leibniz-Institut für Ostseeforschung Warnemünde unter der Betreuung von Herrn Dr. Martin Schmidt. Für die gute Betreuung und die vielen Anregungen und Hinweise auf interessante, forschungsrelevante Themen möchte ich mich bedanken.
Außerdem möchte ich mich bei Dr. René Friedland, Herrn Prof. Thomas Neumann, Herrn Dr. Hagen Ratke, Frau Dr. Anja Eggert, Herrn Dr. Ivan Kuznetsov und Herrn Dr. Tim Junker für Anregungen und Diskussionen bezüglich meiner Arbeit bedanken.
Clemens Krautschick, Ronja Ebner und Maria Oskarsson verdanke ich viele Korrekturen und Verbesserungsvorschläge von Fehlern, die sie beim Lesen des Entwurfes dieser Arbeit entdeckt haben. Danke!

6 Eidesstattliche Erklärung

Ich erkläre hiermit an Eides statt, dass ich die vorliegende Arbeit selbständig und ohne unerlaubte fremde Hilfe angefertigt, und andere als die angegebenen Quellen und Hilfsmittel nicht benutzt habe. Die aus fremden Quellen direkt oder indirekt übernommenen Stellen sind als solche kenntlich gemacht.
Die Arbeit wurde bisher in gleicher oder ähnlicher Form keinem anderen Prüfungsamt vorgelegt und auch nicht veröffentlicht.

Ort, Datum Unterschrift

7 Annex

7.1 Bessel Integrals

$\int xJ_0(x)\mathrm{d}x = xJ_1(x);\ \int xY_0(x)\mathrm{d}x = xY_1(x)$
$\int xI_0(x)\mathrm{d}x = xI_1(x);\ \int xK_0(x)\mathrm{d}x = -xK_1(x)$

7.2 Detailed derivations of equations in section 2

Pressure perturbation for the wind patch (section 2.7.2):

$$
\begin{aligned}
p(r,\varphi,t) &= \int_{-\infty}^{\infty}\int_{0}^{\infty}\sum_{m=-\infty}^{\infty} r' G_m(r,r') F(r',\varphi,\omega) e^{im\varphi - i\omega t}\mathrm{d}r'\mathrm{d}\omega \\
&= \int_{-\infty}^{\infty}\gamma\int_{0}^{\infty}\sum_{m=-\infty}^{\infty} G_m(r,r')\theta(r_0-r') \\
&\quad \left[-i\omega\frac{\partial}{\partial r'}r'R - m\omega\phi + f\frac{\partial}{\partial r'}r'\phi + imfR\right] e^{im\varphi - i\omega t}\mathrm{d}r'\mathrm{d}\omega \\
&= \int_{-\infty}^{\infty}\gamma\int_{0}^{\infty}\sum_{m=-\infty}^{\infty} G_m(r,r')\theta(r_0-r')\left[-i\omega R - m\omega\phi + f\phi + imfR\right] e^{im\varphi - i\omega t}\mathrm{d}r'\mathrm{d}\omega \\
&\quad -\int_{-\infty}^{\infty}\gamma\int_{0}^{\infty}\sum_{m=-\infty}^{\infty} G_m(r,r')\delta(r_0-r')\Big[fr'\phi - i\omega r' R\Big] e^{im\varphi - i\omega t} dr' d\omega \\
&= \int_{-\infty}^{\infty} 2\gamma\frac{u_*^2}{h_n}\frac{i}{\omega}\pi\int_{0}^{\infty}\left[i\omega\sin(\varphi) - i\omega\sin(\varphi) + f\cos(\varphi) - f\cos(\varphi)\right] e^{-i\omega t} dr' d\omega \ (*Ansatz\, n.) \\
&\quad -\int_{-\infty}^{\infty}\gamma\sum_{m=-\infty}^{\infty} G_m(r,r_0)\Big[fr_0\phi - i\omega r_0 R\Big] e^{im\varphi - i\omega t} d\omega \\
&= -\int_{-\infty}^{\infty}\gamma\sum_{m=-\infty}^{\infty} G_m(r,r_0)\Big[fr_0\phi - i\omega r_0 R\Big] e^{im\varphi - i\omega t}\mathrm{d}\omega \\
&= -\frac{u_*^2}{h_n}\int_{-\infty}^{\infty}\gamma G_1(r,r_0)\frac{i\pi}{\omega}\Big[2fr_0\cos(\varphi) + 2i\omega r_0\sin(\varphi)\Big] e^{-i\omega t} d\omega \\
&= \frac{u_*^2}{h_n}\int_{-\infty}^{\infty} G_1(r,r_0)\frac{1}{\omega^2}\frac{1r_0}{\lambda\sqrt{f^2-\omega^2}}\Big[f\cos(\varphi) + i\omega\sin(\varphi)\Big] e^{-i\omega t} d\omega \\
&= \frac{u_*^2}{h_n}\int_{-\infty}^{\infty} G_1(r,r_0)\frac{\rho_0}{\omega^2}\Big[f\cos(\varphi) + i\omega\sin(\varphi)\Big] e^{-i\omega t} d\omega \\
&\quad N\ddot{a}herung \\
&= \frac{u_*^2}{h_n}\rho_0\int_{-\infty}^{\infty}\frac{1}{\omega^2} G_1(\lambda f\rho, \lambda f\rho_0)\Big[f\cos(\varphi) + i\omega\sin(\varphi)\Big] e^{-i\omega t} d\omega \\
&= \theta(t)\frac{u_*^2}{h_n}\rho_0\left[\theta(\rho-\rho_0) I_1(\lambda f\rho_0) K_1(\lambda f\rho) + \theta(\rho_0-\rho) K_1(\lambda f\rho_0) I_1(\lambda f\rho)\right]\Big[\sin(\varphi) - tf\cos(\varphi)\Big]
\end{aligned}
$$

Pressure perturbation for the lateral linear increasing wind field (section 2.7.3):

$$\begin{aligned}
p(r,\varphi) &= \int_0^\infty r' G(r,r') F(r',\varphi) dr' \\
&= -\frac{1}{i\tilde{\omega}} \frac{f}{\lambda\sqrt{f^2-\omega^2}} \frac{\Phi_*^2}{h_n} \frac{i}{\omega+i\epsilon} \int_0^\infty G(r,r') \left[\left(\frac{\partial_{r'} r'^2}{\lambda\sqrt{f^2-\omega^2}} \theta(r_0-r') \right) \right] dr' \\
&= \frac{f}{\lambda^2(f^2-\omega^2)} \frac{\Phi_*^2}{h_n} \frac{-1}{\omega^2+2i\omega\epsilon-\epsilon^2} \int_0^\infty G(r,r') \left[(\partial_{r'} r'^2 \theta(r_0-r')) \right] dr' \\
&= \underbrace{\frac{f}{\lambda^2(f^2-\omega^2)} \frac{\Phi_*^2}{h_n} \frac{-1}{(\omega+i\epsilon)^2}}_{\gamma_2} \int_0^\infty G(r,r') \left[2r'\theta(r_0-r') - r'^2 \delta(r_0-r') \right] dr'
\end{aligned}$$

Case differentiation:

$$G \star r'\theta(r-r') = \theta(r-r_0) \int_0^{r_0} dr' r' G^>(r,r') + \theta(r_0-r) \left[\int_0^r dr' r' G^>(r,r') + \int_r^{r_0} dr' r' G^<(r,r') \right]$$

For the integrals, the formulas from section 7.1 are used.

$$\begin{aligned}
p(r,\varphi,\omega) &= \gamma_2 \int_0^\infty G(r,r') \left[2r'\theta(r_0-r') - r'^2\delta(r_0-r') \right] dr' \\
&= 2\gamma_2\theta(r-r_0) K_0(r) \int_0^{r_0} dr' r' I_0(r') \\
&\quad + 2\gamma_2\theta(r_0-r) \left[K_0(r) \int_0^r dr' r' I_0(r') + I_0(r) \int_r^{r_0} dr' r' K_0(r') \right] \\
&\quad - \gamma_2 r_0^2 \left[\theta(r-r_0) I_0(r_0) K_0(r) + \theta(r_0-r) K_0(r_0) I_0(r) \right] \\
&= 2\gamma_2\theta(r-r_0) r_0 K_0(r) I_1(r_0) + 2\gamma_2\theta(r_0-r) \left[r K_0(r) I_1(r) - r_0 I_0(r) K_1(r_0) + r I_0(r) K_1(r) \right] \\
&\quad - \gamma_2 r_0^2 \left[\theta(r-r_0) I_0(r_0) K_0(r) + \theta(r_0-r) K_0(r_0) I_0(r) \right] \\
&= \gamma_2\theta(r_0-r) \left[2r K_0(r) I_1(r) - 2r_0 I_0(r) K_1(r_0) + 2r I_0(r) K_1(r) - r_0^2 K_0(r_0) I_0(r) \right] \\
&\quad + \gamma_2\theta(r-r_0) \left[2r_0 K_0(r) I_1(r_0) - r_0^2 I_0(r_0) K_0(r) \right] \\
&= \gamma_2\theta(r_0-r) \left[2r \left(\frac{1}{r} \right) - r_0^2 I_0(r) \left(\frac{2}{r_0} K_1(r_0) + K_0(r_0) \right) \right] \\
&\quad + \gamma_2\theta(r-r_0) \left[r_0^2 K_0(r) \left(\frac{2}{r_0} I_1(r_0) - I_0(r_0) \right) \right]
\end{aligned}$$

Pressure perturbation for the conineous wind field (section 2.7.4):

$$
\begin{aligned}
p(r,\varphi,t) &= \int_{-\infty}^{\infty}\gamma\int_0^{\infty}\Sigma_{-\infty}^{\infty}G_m(r,r')\left(f\frac{\partial}{\partial r}r'\phi\right)e^{im\varphi-i\omega t}\mathrm{d}r'\mathrm{d}\omega\\
&= \frac{u_*^2}{h_n}2\pi i\int_{-\infty}^{\infty}\frac{\gamma}{\omega}\int_0^{\infty}G_0(r,r')\left(f\frac{\partial}{\partial r}r'r'e^{-r'}\right)e^{-i\omega t}\mathrm{d}r'\mathrm{d}\omega\\
&= -\frac{u_*^2}{h_n}\frac{1}{\lambda}\int_{-\infty}^{\infty}\frac{1}{\omega^2}\int_0^{\infty}G_0(r,r')\left(2r'-r'^2\right)e^{-r'}e^{-i\omega t}\mathrm{d}r'\mathrm{d}\omega\\
&= \frac{u_*^2}{h_n}\frac{1}{\lambda}\theta(t)t\int_0^{\infty}G_0(r,r')f\left(2r'-r'^2\right)e^{-r'}\mathrm{d}r'\\
&= \frac{u_*^2}{h_n}\frac{1}{\lambda}\theta(t)tK_0(r)\int_0^{r}I_0(r')f\left(2r'-r'^2\right)e^{-r'}\mathrm{d}r'\\
&+ \frac{u_*^2}{h_n}\frac{1}{\lambda}\theta(t)tI_0(r)\int_r^{\infty}K_0(r')f\left(2r'-r'^2\right)e^{-r'}\mathrm{d}r'\\
&= \frac{u_*^2}{h_n}\frac{1}{\lambda}\theta(t)tK_0(r)\Bigg(\left[\frac{2r'e^{-r'}}{3}\left[r'I_0(r')+(1+r')I_1(r')\right]\right]_0^{r}\\
&- \left[\frac{r'e^{-r'}}{15}\left[(-2r'+3r'^2)I_0(x)+(4+4r'+3r'^2)I_1(r')\right]\right]_0^{r}\Bigg)\\
&+ \frac{u_*^2}{h_n}\frac{1}{\lambda}\theta(t)tI_0(r)\Bigg(\left[\frac{2r'e^{-r'}}{3}\left[r'K_0(r')-(1+r')K_1(r')\right]\right]_r^{\infty}\\
&- \left[\frac{r'e^{-r'}}{15}\left[(+3r'^2-2r')I_0(x)-(4+4r'+3r'^2)I_1(r')\right]\right]_r^{\infty}\Bigg)\\
&= \frac{u_*^2}{h_n}\frac{1}{\lambda}\theta(t)tK_0(r)\Bigg(\left[\frac{2re^{-r}}{3}\left[rI_0(r)+(1+r)I_1(r)\right]\right]\\
&- \left[\frac{re^{-r}}{15}\left[(3r^2-2r)I_0(r)+(4+4r+3r^2)I_1(r)\right]\right]\Bigg)\\
&- \frac{u_*^2}{h_n}\frac{1}{\lambda}\theta(t)tI_0(r)\Bigg(\left[\frac{2re^{-r}}{3}\left[rK_0(r)-(1+r)K_1(r)\right]\right]\\
&- \left[\frac{re^{-r}}{15}\left[(3r^2-2r)K_0(r)-(4+4r+3r^2)K_1(r)\right]\right]\Bigg)\\
&= \frac{u_*^2}{h_n}\frac{1}{\lambda}\theta(t)t\frac{2re^{-r}}{3}\left((1+r)\left(K_0(r)I_1(r)+I_0(r)K_1(r)\right)\right)\\
&- \frac{u_*^2}{h_n}\frac{1}{\lambda}\theta(t)t\frac{re^{-r}}{15}\left((4+4r+3r^2)\left(I_0(r)K_1(r)+K_0(r)I_1(r)\right)\right)\\
&= \frac{u_*^2}{h_n}\frac{1}{\lambda}\theta(t)t\frac{1}{15}e^{-r}\left(3r^2-6r-6\right)\\
p(\rho,\varphi,t) &= \frac{u_*^2}{h_n}\frac{1}{\lambda}\theta(t)t\frac{1}{15}e^{-\lambda f\rho}\left(3(\lambda f\rho)^2-6\lambda f\rho-6\right)
\end{aligned}
$$